Front. Earth Sci. 2023, 17(1): 273–292
https://doi.org/10.1007/s11707-022-0988-z

RESEARCH ARTICLE

Water-bearing characteristics and their effects on the nanopores of overmature coal-measure shales in the Wuxiang area of the Qinshui Basin, north China

Peng CHENG[1,2], Xianming XIAO (✉)[3], Hui TIAN[1,2], Jian SUN[3], Qizhang FAN[3], Haifeng GAI[1,2], Tengfei LI[1,2]

1 State Key Laboratory of Organic Geochemistry, Guangzhou Institute of Geochemistry, Chinese Academy of Sciences, Guangzhou 510640, China
2 CAS Center for Excellence in Deep Earth Science, Guangzhou 510640, China
3 School of Energy Resources, China University of Geosciences (Beijing), Beijing 100083, China

Abstract In this study, a group of overmature coal-measure shale core samples was collected *in situ* from an exploration well located in the Wuxiang area of the Qinshui Basin, north China. The pore water contents (C_{PW}) of the shales under as-received conditions, equilibrium water contents (C_{EW}) of the shales under moisture equilibrium conditions (relative humidity: 100%), and nanopore structures of the shales under both as-received and dried conditions were measured. The results indicate that the C_{PW} values of these shales are much lower than their C_{EW} values, which implies that the bulk pore systems of these shales have low water-bearing extents. In addition, approximately half of the total pore volumes and surface areas of the as-received shales are occupied by pore water, and the effects of pore water on shale nanopores with various pore types and widths are different. The average water-occupied percentages (P_W) are 59.16%–81.99% and 42.53%–43.44% for the non-micropores and micropores, respectively, and are 83.54%–97.69% and 19.57%–26.42% for the inorganic-matter hosted (IM) and organic-matter hosted (OM) pores, respectively. The pore water in shales not only significantly reduces the storage of shale gas by occupying many pore spaces, but also causes the shale gas, especially the absorbed gas, to be mostly stored in the OM pores; meanwhile, the IM pores mainly store free gas. Therefore, the water-bearing characteristics and their effects on the pore structures and gas-bearing properties of coal-measure shales should be noted for the evaluation and exploration of shale gas in the Qinshui Basin.

Keywords coal-measure shales, water-bearing characteristics, nanopore structures, shale gas, the Qinshui Basin

Received November 17, 2021; accepted March 10, 2022

E-mail: xmxiao@cugb.edu.cn

1 Introduction

Although organic-rich shales with shale gas potential developed widely in marine, marine-terrestrial transitional and terrestrial strata in China, only marine shale gas has achieved commercial development presently (Zhang et al., 2009; Jia et al., 2012; Guo, 2016; Zou et al., 2016; Zou et al., 2020a). The total shale gas production in China reached 200 × 10^8 m^3 in 2020, and 99% of this production was provided by the Lower Palaeozoic marine shales (Men et al., 2021). At present, however, the exploration and development of nonmarine shale strata are still in an early stage, and coal-measure shales are regarded as important potential exploration targets following marine shales (Dong et al., 2016b).

Gas-bearing marine shales generally contain certain levels of pore water, and the water saturations of commercial shale gas plays are generally lower than 45%, such as 25%–30%, 15%–20%, 15%–35%, and 30%–45% for the Barnett, Haynesville, Fayetteville and Longmaxi shale gas plays, respectively (Boyer et al., 2006; Cipolla et al., 2010; Wu and Aguilera, 2012; Fang et al., 2014; Wei and Wei, 2014). However, shale gas plays with water saturations greater than 45% generally have low shale gas yields, e.g., the Zhaotong shale gas plays in the Sichuan Basin, south China (Liu and Wang, 2013). Because substantial amounts of pore water have been expelled from shale pore systems due to the compaction of overlying strata and by displacement drainage of the generated hydrocarbons during the diagenetic and thermal evolution stages (Wardlaw and McKellar, 1998;

Mahadevan et al., 2007; Cheng et al., 2019), the bulk pore systems of highly mature or overmature shales generally have low water-bearing extents. These shales may barely contain free liquid water, and most of the pore water is confined to the nanopores or is adsorbed on their inner surfaces (Bennion and Thomas, 2005; Cheng et al., 2017, 2018).

Pore water and shale gas are concomitantly stored in the pore systems of gas shales, and thus the water-bearing characteristics of shales significantly affect their gas-bearing properties (Ambrose et al., 2010; Sondergeld et al., 2010; Gasparik et al., 2014; Merkel et al., 2015; Yang et al., 2020). Under certain geological conditions, the contents, distributions and occurrences of pore water are closely related to the pore types and widths of shale nanopores (McCutcheon and Barton, 1999; Passey et al., 2010; Wen et al., 2015; Li et al., 2016; Zolfaghari et al., 2017; Feng et al., 2018; Chen et al., 2019). It is generally believed that pore water is dominantly stored in the inorganic-matter hosted (IM) pores of shales, while the organic-matter hosted (OM) pores barely contain water, because the inorganic matter surfaces are hydrophilic and the organic matter surfaces are hydrophobic (Passey et al., 2010; Sondergeld et al., 2010; Odusina et al., 2011; Korb et al., 2014; Zolfaghari et al., 2017; Zou et al., 2020b). However, the wettability of organic matter is still unclear and may depend on its maturity and kerogen type (Bekyarova et al., 2002; Charrière and Behra, 2010; Hu et al., 2015, 2016; Gu et al., 2016; Gao et al., 2019). For the same type of shale nanopores, pore water preferentially occupies nanopores with small pore widths, because they have stronger capillary forces than nanopores with large pore widths (Striolo et al., 2005; Li et al., 2017; Wu et al., 2017).

Although logging data are generally used to calculate the water saturations of gas shale reservoirs during the exploration and development of shale gas, this method is inadequate for exactly recognizing the contents, distributions and occurrences of pore water in various shale nanopores (Miller and Shanley, 2010; Wu and Aguilera, 2012). Therefore, an increasing number of laboratory studies have performed on as-received shales to investigate their water-bearing characteristics (Cheng et al., 2017; Sun et al., 2020a, 2020b). However, few of these laboratory studies have been conducted on as-received coal-measure shales. Coal-measure and marine shales are quite different in geological and geochemical characteristics. For example, compared with marine shales, coal-measure shales are richer in terrestrial macerals and have fewer OM pores and wider ranges of GIP contents (De Silva et al., 2015; Jiang et al., 2017; Yang et al., 2017; Zhang et al., 2019b). Therefore, the two types of shales should exhibit diverse water-bearing characteristics and pore structures. At present, the water-bearing characteristics and their effects on nanopore structures are still unclear for coal-measure shales, and this is one of the important reasons that has limited their shale gas development.

The Upper Carboniferous and Lower Permian coal-measure shales developed extensively in the Qinshui Basin, north China (Cai et al., 2011; Dong et al., 2016a; Li et al., 2018; Liang et al., 2018; Zhang et al., 2019a; Liang et al., 2020), and they were expected to have high shale gas potential with a geological resource of more than 2.93×10^{12} m^3 (Liu, 2016). Recently, a few exploration wells that targeted these strata were drilled in the Wuxiang area of the basin, and a group of gas-bearing shale core samples were collected in situ at the drilling sites. The pore water contents (C_{PW}) of the shales under as-received conditions, equilibrium water contents (C_{EW}) of the shales under moisture equilibrium conditions (relative humidity: 100%) and nanopore structures of the shales under both as-received and dried conditions were investigated in this study. The results of this study preliminarily reveal the water-bearing characteristics and their effects on the nanopore structures of overmature coal-measure shales, which may promote accurate evaluations of their gas-bearing properties.

2 Geological background

The Qinshui Basin is located in the north China Craton and is delimited by Taihang Mountain in the east, Zhongtiao Mountain in the south, Huo Mountain in the west and Wutai Mountain in the north (Fig. 1(a)). The basin has an area of 3×10^4 km^2 and spans 120 km in the east–west direction and 330 km in the north–south direction. The strata in the Qinshui Basin were stably and continuously deposited during the Hercynian period, gently uplifted during the Indosinian period, and intensely uplifted during the Yanshan period. The final structural framework of this basin was formed at the end of the Yanshan period, and this basin remained structurally stable after this period (Ren et al., 2005; Song et al., 2019).

The marine-terrestrial transitional strata in the Qinshui Basin were deposited during the late Palaeozoic (Fig. 1(b)). The Lower Carboniferous Benxi Formation, with a thickness of 0–75 m, was deposited in a carbonate tidal flat environment and contains mainly gray aluminous mudstones with a few thin coal and sandstone seams. The Upper Carboniferous Taiyuan Formation, with a thickness of 50–135 m, was deposited in a barrier bar environment and contains mainly black shales, sandy mudstones, sandstones and coal seams. The Lower Permian Shanxi Formation, with a thickness of 20–90 m, was deposited in a delta front environment and contains mainly shales, sandstones, and sandy mudstones with coal seams. The Upper Permian and Triassic strata, with thicknesses of 1350–2150 m, were deposited mainly in fluvial and lacustrine environments, and they are

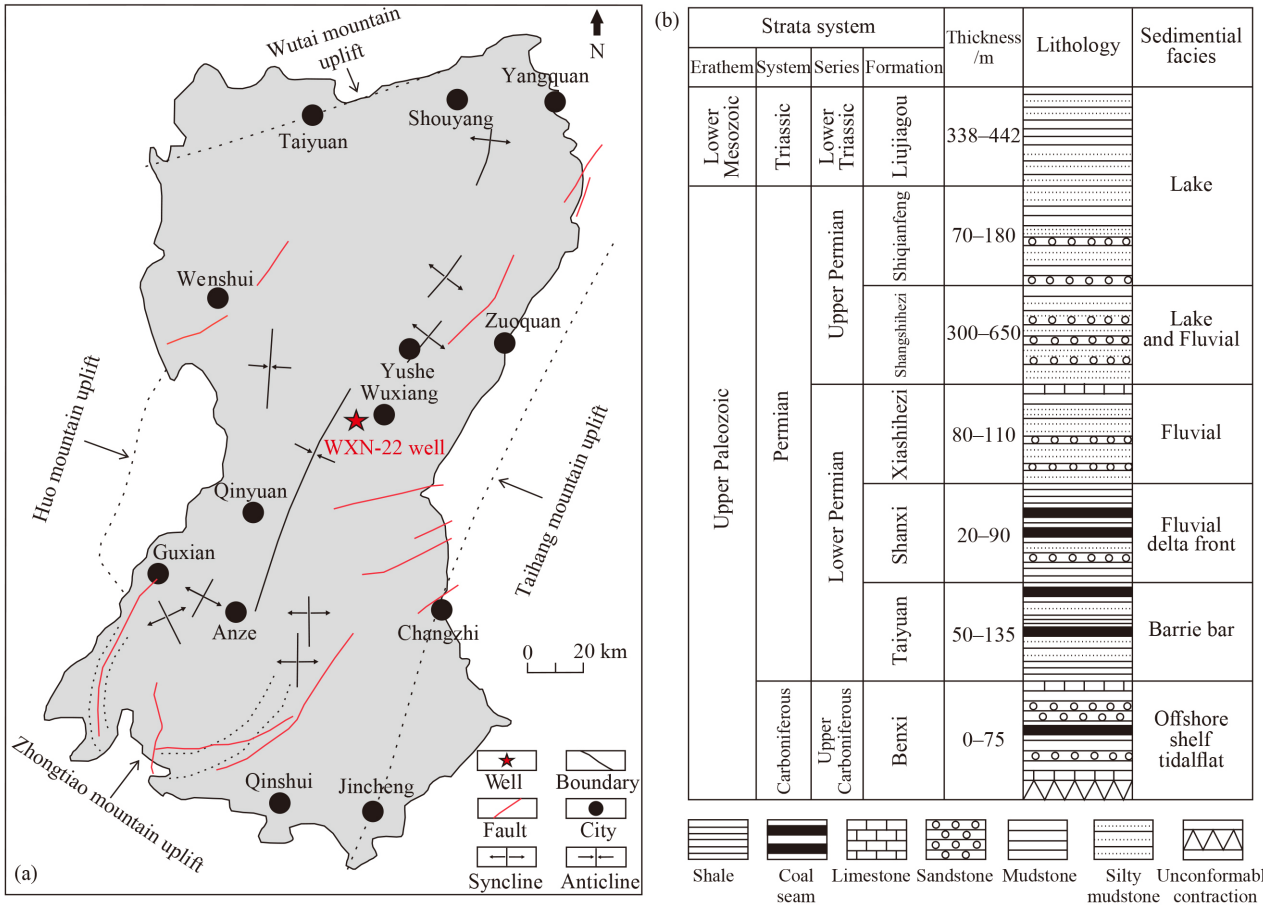

Fig. 1 Schematic image showing the structural framework of the Qinshui Basin (a) and the stratigraphic column of the marine-continental transitional strata in this basin (b) (modified after Su et al., 2005).

composed of thick silty mudstones and gray mudstones. In the Qinshui Basin, the shales and coals in the Taiyuan and Shanxi Formations were the main source rocks, and the silty and gray mudstones in the Upper Permian and Triassic strata were the main cap rocks (Fig. 1(b)). Coalbed gas, shale gas, and tight sandstone gas coexist in this basin (Su et al., 2005; Cai et al., 2011; Qin et al., 2014; Song et al., 2019; Liang et al., 2020).

3 Method, samples and experiments

3.1 Method

The water saturations of normal oil and gas reservoirs are generally calculated from well logging data; however, this method has low resolution for shale strata and fails to reveal the water distributions and occurrences in various shale nanopores (Miller and Shanley, 2010; Wu and Aguilera, 2012). Therefore, further laboratory analyses on the water-bearing characteristics of as-received shale samples are necessary to obtain this information (Ahmad and Haghighi, 2013; Cheng et al., 2018).

Gas shales generally have low pore water contents, and the water is strongly confined in the shale nanopores, which results in minimal evaporation when the shale samples are sealed and preserved at room temperature (Handwerger et al., 2011). The shale plunger samples used in this study were drilled from the inner part of shale core samples to eliminate the influences of drilling muds. In addition, all the selected shale samples contained shale gases which largely prevented drilling muds from immersing into the shale pore systems (Cheng et al., 2018). Therefore, gas-bearing shale samples, which are directly pretreated at drilling sites after being recovered from wells and preserved in plastic bags as soon as possible, are commonly used in laboratory studies, and the pore water content (C_{PW}) of the as-received shale samples can represent the approximate water contents under geological conditions (Hartman et al., 2008; Gensterblum et al., 2013; Korb et al., 2014). The equilibrium water content (C_{EW}) of a shale sample, which is measured when the shale has reached the moisture equilibrium state in an environment of 100% relative humidity, can represent its approximate maximum confined water content. In this study, the ratio of C_{PW} to C_{EW} is defined as the pore water equilibrium extent (E_{PW}) of shales, and the E_{PW} is used to approximately

characterize the water-bearing extents of shales under geological conditions. The C_{PW}, C_{EW}, and E_{PW} values are used in this study to characterize the water-bearing characteristics of shales, and the differences in pore structures of the shales under as-received and dried conditions are applied to reveal the effects of pore water on shale nanopores. The main procedures of the method used in this study are shown in Fig. 2.

3.2 Sample preparations

A total of 12 fresh coal-measure shale core samples (Table 1) were collected *in situ* from the WXN-22 well in the Wuxiang area of the Qinshui Basin (Fig. 1(a)). The collection and preparation procedures for the as-received shale samples are described below. After the full-size shale cores were taken out of the well, they were immediately broken into large blocks, and one of these blocks was immersed in water to determine whether it contained gas. Shale samples with blocks strongly bubbled in water were collected. Only the blocks from the inner parts of the gas-bearing shale cores were used to drill small plunger samples with 20 mm lengths and 15 mm diameters, and the small plunger samples were sealed in plastic bags and transported as soon as possible to the laboratory for analysis.

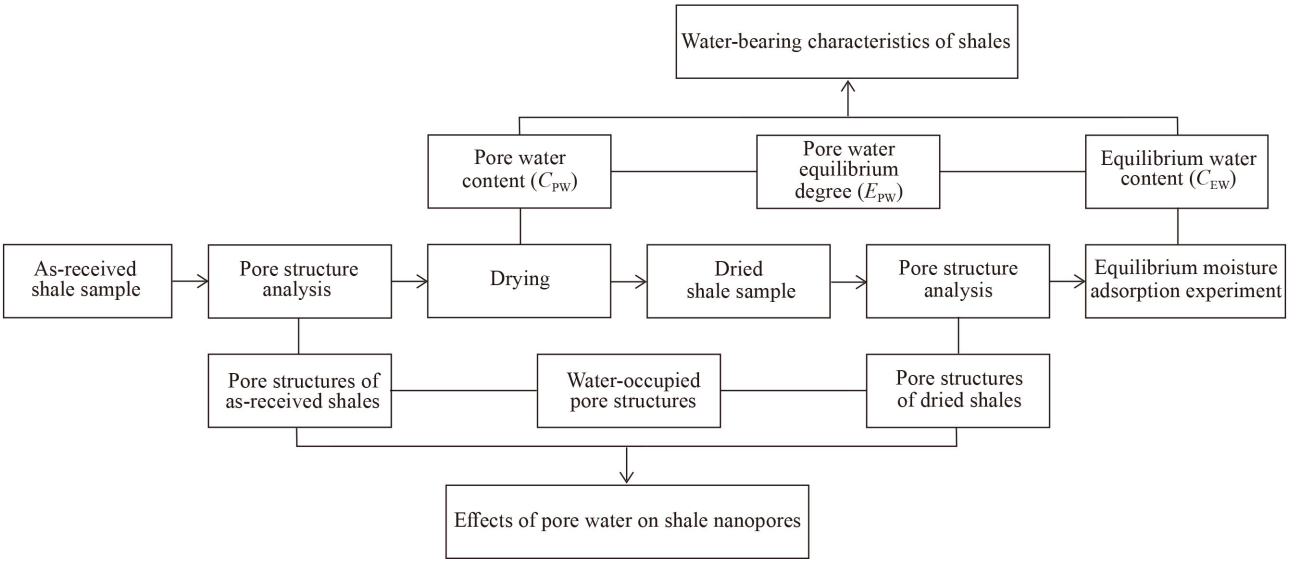

Fig. 2 The sketch map showing the method and its main procedures in this study.

Table 1 Geological, geochemical, and mineralogical data of the studied coal-measure shales

Sample No.	Depth/m	Formation	Lithology	R_o/%	TOC /wt%	Rock-eval			Mineral compositions/wt.%					
						T_{max} /°C	HI/ (mg·g^{-1} TOC)	OI/ (mg·g^{-1} TOC)	Quartz	Feldspar	Clay	Pyrite	Anatase	Dolomite
WXN22-1	1880.6	Shanxi	Shale	—	2.55	590	14	5	45.0	2.0	49.2	1.4	2.4	0.0
WXN22-2	1891.3	Shanxi	Shale	3.29	2.31	595	14	10	47.0	3.1	34.0	4.7	2.1	9.1
WXN22-3	1901.1	Shanxi	Shale	—	10.06	594	13	2	22.6	2.4	71.1	1.4	2.5	0.0
WXN22-4	1910.1	Shanxi	Shale	—	4.43	605	10	4	35.7	2.0	58.4	2.3	1.6	0.0
WXN22-5	1922.1	Shanxi	Shale	3.36	3.90	603	7	6	37.4	2.9	50.4	7.6	1.7	0.0
WXN22-6	1930.4	Shanxi	Shale	—	3.76	599	13	5	46.0	2.7	37.9	6.2	2.0	5.2
WXN22-7	1933.2	Shanxi	Shale	—	7.98	606	6	2	35.7	1.7	46.9	13.9	1.8	0.0
WXN22-8	1939.7	Shanxi	Shale	3.32	3.43	597	12	10	33.9	2.4	56.1	7.6	0.0	0.0
WXN22-9	1967.1	Taiyuan	Shale	—	13.82	600	25	2	53.0	0.0	43.8	0.6	2.6	0.0
WXN22-10	1971.9	Taiyuan	Shale	—	1.33	596	14	17	32.8	1.1	57.7	6.6	1.8	0.0
WXN22-11	1986.6	Taiyuan	Shale	3.40	3.08	605	6	2	31.1	0.7	62.2	5.0	1.0	0.0
WXN22-12	2010.5	Taiyuan	Shale	—	6.82	605	11	12	17.4	0.0	71.9	10.7	0.0	0.0

3.3 Experiments

3.3.1 Pore water and equilibrium water measurements

A prepared small plunger shale sample was directly weighed to obtain its as-received mass (m_{AR}, g). After being dried for 12 h in a vacuum oven at a temperature of 105°C and a pressure of < 30 mmHg, the shale samples were weighed again to obtain their dried mass (m_{Dry}, g). The pore water content (C_{PW}, mg/g) of the sample was calculated using Eq. (1):

$$C_{PW} = [(m_{AR} - m_{Dry}) \times 1000]/m_{Dry}. \quad (1)$$

Then, the dried shale sample was further used in an equilibrium moisture adsorption experiment by following the recommended method from the American Society for Testing and Materials (ASTM D1412-07, 2010). The experimental procedures have been adequately described in previous literature (e.g., Ross and Bustin, 2009; Cheng et al., 2017; Zolfaghari et al., 2017) and are briefly summarized here. The shale samples were placed on the platform of a vacuum desiccator, and the bottom of the desiccator was filled with deionized water to maintain its inner environment at a relative humidity of 100% (Zhang et al., 2004). The desiccator was then placed in a water bath at a temperature of 30°C, and the absolute pressure in the desiccator was evacuated to < 30 mmHg. The moist shale samples were weighed at 12 h intervals, and their pore systems were considered to have reached the moisture equilibrium state when the weighed mass remained constant (m_{CE}, g). Based on the m_{Dry} and m_{CE} values, the equilibrium water content (C_{EW}, mg/g) of the shale was calculated using Eq. (2). Then, the pore water equilibrium extent (E_{PW}, %) of each shale sample was further calculated using Eq. (3).

$$C_{EW} = [(m_{CE} - m_{Dry}) \times 1000]/m_{Dry}, \quad (2)$$

$$E_{PW} = C_{PW}/C_{EW} \times 100\%. \quad (3)$$

3.3.2 Mineralogical analysis

The mineralogical composition analyses were based on dried shale powder samples using granularities of < 75 μm (i.e., < 200 mesh) and were conducted with an X-ray diffractometer (Bruker D8 Advance XRD instrument). The measurements were performed at 40 kV and 30 mA with Cu Kα radiation, and stepwise scanning was performed at a rate of 4°/min that ranged between 3° and 85° (2θ). Based on the peak area of each mineral, the mineralogical compositions of the shales were semiquantitatively estimated and corrected by the Lorentz-polarization method (Chalmers and Bustin, 2008). The average value of two XRD measurements for each sample was used.

3.3.3 Pore structure analysis

The International Union of Pure and Applied Chemistry (IUPAC) generally classifies shale nanopores into micropores (< 2 nm), mesopores (2−50 nm), and macropores (> 50 nm) (Chalmers et al., 2009). This study approximately characterized the micropores and non-micropores (including mesopores and macropores) by using low-pressure CO_2 and N_2 adsorption experiments, respectively. Shale grain samples with granularities of 380–830 μm (20–40 mesh) were used to carry out adsorption experiments by a Micromeritics ASAP 2020^M instrument. The CO_2 adsorption experiment was performed at a temperature of 0°C in an ice-water mixture environment, while the N_2 adsorption experiment was carried out at a temperature of –196.56°C in a liquid nitrogen environment. The relative pressures of the CO_2 and N_2 adsorption experiments are 0.00001–0.032 and 0.005–0.995, respectively. Before the gas adsorption experiments, the dried shale samples were degassed in situ for 6 h at a temperature of 105°C and a pressure of lower than 10 mmHg to further eliminate the potential influences of moisture in the ambient environment (Bustin et al., 2008). However, instead of the degassing procedure, the as-received shale samples in the testing apparatus were directly stored in an ice-water mixture or a liquid nitrogen environment prior to the CO_2 or N_2 adsorption experiments to prevent the potential evaporation losses of their pore water (Cheng et al., 2018, 2019). The micropore surface areas (S_{mic}) and pore volumes (V_{mic}) were obtained by using the CO_2 adsorption data according to the Dubinin-Astakhov equation (Dubinin, 1989). The non-micropore surface areas (S_{non}) were obtained by using the N_2 adsorption data based on the modified Brunauer–Emmett–Teller equation (Brunauer et al., 1938; Tian et al., 2015), and the non-micropore pore volumes (V_{non}) were calculated on maximum N_2 adsorption quantities.

4 Results and discussion

4.1 Geochemical and mineralogical characteristics of the studied shales

The geochemical and mineralogical data for the studied shales are presented in Table 1. The TOC contents of the shales have a wide range of 1.33−13.82 wt.%, and the R_o and T_{max} values are 3.29%−3.40% and 590°C−606°C, respectively, which indicates that these shales have evolved to an overmature stage (Table 1). The shales have low HI and OI values in the ranges of 6−25 mg/g TOC and 2−17 mg/g TOC, respectively (Table 1).

The main minerals of the shales include clays, quartz, and pyrite, with contents of 34.0−71.9 wt.%, 17.4−53.0 wt.%, and 0.6−13.9 wt.%, respectively (Table 1). In

addition, some shale samples also contain small amounts of feldspar, anatase and dolomite (Table 1). When compared with the marine gas shales from wells FY1, YQ1, and XK2 in the Upper Yangtze area, south China (Cheng et al., 2018; Sun et al., 2020b), the studied shales are richer in clay minerals and scarcer in carbonate minerals.

4.2 Water-bearing characteristics of the studied shales

The C_{PW} and C_{EW} values of the studied shales are 1.99–7.42 mg/g and 19.16–32.90 mg/g, respectively (Table 2). The C_{PW} and C_{EW} values of the shales are closely correlated to their organic and inorganic compositions. Both the C_{PW} and C_{EW} values have positive relationships with the clay contents, and the correlation coefficients (R^2) are 0.56 and 0.42, respectively (Fig. 3(a)); this is mainly because the clays in the shales provide hydrophilic IM pore spaces for water storage (Passey et al., 2010; Wen et al., 2015; Zolfaghari et al., 2017). Except for the WXN22-9 sample, which has a high TOC content and a low clay content (Table 1), the C_{PW} and C_{EW} values of the other samples also exhibit positive relationships with the TOC contents, and the correlation coefficients (R^2) are 0.60 and 0.72, respectively (Fig. 3(b)); this is probably because the organic matter in the shales generally developed OM micropores that could store water due to capillary binding force (Newsham et al., 2003; Liu and Monson, 2005). The C_{PW} and C_{EW} values are negatively correlated with the quartz contents, and the correlation coefficients (R^2) are 0.51 and 0.40, respectively (Fig. 3(c)); this is probably because the quartz in the shales barely developed nanopores and failed to provide pore spaces for water storage. The C_{PW} values are much lower than the C_{EW} values, with E_{PW} values ranging from 9.98% to 23.47% (Table 2), which indicates that the bulk pore systems of the shales have low water-bearing extents. Additionally, the E_{PW} values of the studied shales exhibit positive correlations with the TOC and clay contents and a negative correlation with the quartz content (Table 2 and Fig. 4).

Cheng et al. (2017, 2018) reported that the C_{PW}, C_{EW}, and E_{PW} values of the FY1 and YQ1 overmature Lower Palaeozoic marine shales in the Upper Yangtze area, south China, were 3.70–5.29 mg/g, 8.13–15.04 mg/g, and 34.23%–45.51%, respectively. When compared with marine shales, the studied coal-measure shales have similar C_{PW} values but larger C_{EW} values. The low C_{PW} values for both types of overmature shales may be related to their strong water drainage during thermal evolution stages (Wardlaw and McKellar, 1998; Mahadevan et al., 2007; Cheng et al., 2019). The greater C_{EW} values of the studied shales are attributed to their higher clay contents (Table 1) than the marine shales (17.7–40.4 wt% from Cheng et al., 2017) and to the organic matter, with type III kerogen, present in the coal-measure shales being more hydrophilic than the organic matter, with type II kerogen, present in the marine shales (Gu et al., 2016; Gao et al., 2019). In addition, because the filling extent of pore water in shale pores is significantly determined by pore volumes at high moisture equilibrium conditions (Seemann et al., 2017; Chen et al., 2021), the studied shales have larger total pore volumes than marine shales, which may also account for their higher C_{EW} values.

4.3 Pore structure characteristics of the studied shales

4.3.1 Micropores and non-micropores

The pore surfaces and volumes of the studied shales

Table 2 Pore water contents (C_{PW}), equilibrium water contents (C_{EW}) and pore water equilibrium extents (E_{PW}) of the studied coal-measure shales

Sample No.	Depth/m	Formation	Water-bearing characteristics		
			Pore water content/ ($mg \cdot g^{-1}$)	Equilibrium water content/ ($mg \cdot g^{-1}$)	Pore water equilibrium extent/%
WXN22-1	1880.6	Shanxi	2.16	19.16	11.25
WXN22-2	1891.3	Shanxi	1.99	19.98	9.98
WXN22-3	1901.1	Shanxi	7.42	32.90	22.55
WXN22-4	1910.1	Shanxi	4.47	24.56	18.21
WXN22-5	1922.1	Shanxi	4.13	23.92	17.28
WXN22-6	1930.4	Shanxi	2.82	23.22	12.12
WXN22-7	1933.2	Shanxi	5.05	23.69	21.32
WXN22-8	1939.7	Shanxi	4.56	21.21	21.49
WXN22-9	1967.1	Taiyuan	4.87	23.83	20.44
WXN22-10	1971.9	Taiyuan	4.82	21.93	21.99
WXN22-11	1986.6	Taiyuan	3.56	23.29	15.29
WXN22-12	2010.5	Taiyuan	6.25	26.62	23.47

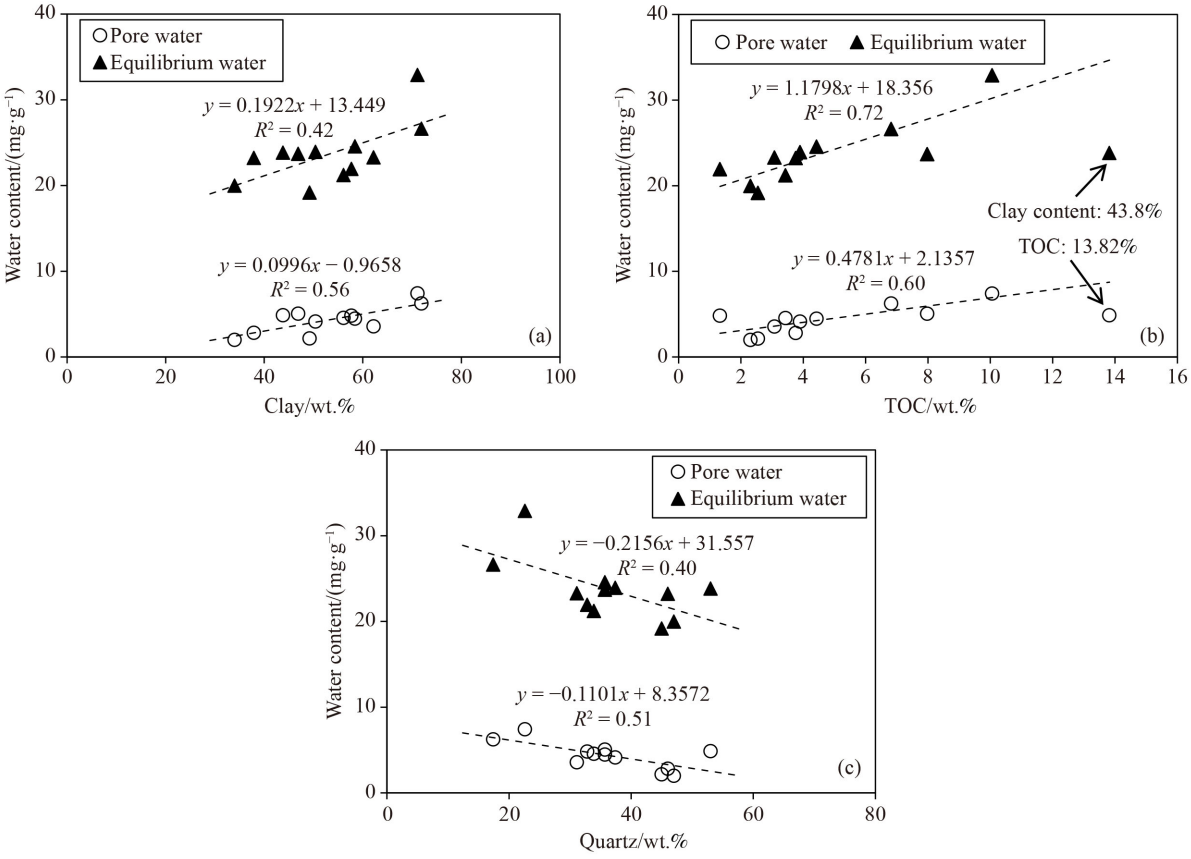

Fig. 3 Correlations of the pore water and equilibrium water contents with the clay (a), TOC (b), and quartz contents (c) for the studied coal-measure shales.

under as-received conditions are listed in Table 3. These data indicate that the pore surface areas of the as-received shales are dominantly provided by micropores, while their pore volumes are co-controlled by micropores and non-micropores (Table 3). The pore surfaces and volumes of the micropores and total pores have positive relationships with the TOC contents, with correlation coefficients (R^2) ranging from 0.93 to 0.96 (Figs. 5(a), 5(c), 5(d), 5(f)), while those of the non-micropores show no obvious correlations with the TOC contents (Figs. 5(b) and 5(e)). The pore surfaces and volumes of all of the pores have no obvious relationships with the clay contents (Fig. 6).

The pore surfaces and volumes of the studied shales significantly increase after they are dried (Table 3). The pore surface areas of the dried shales are still mainly provided by the micropores, while their pore volumes are dominantly contributed by the non-micropores (Table 3). The pore surfaces and volumes of the micropores, non-micropores and total pores have positive relationships with the TOC contents, with correlation coefficients (R^2) ranging from 0.65 to 0.97 (Fig. 5). Meanwhile, these parameters also have weakly positive correlations with the clay contents, except for sample WXN22-9 (Fig. 6).

The pore structures of the dried shales differ significantly from those of the as-received shales, and the differences in pore structures of the shales under the two conditions can indicate the extent of influence of pore water on the effective pore structures for the storage of shale gas (see Section 4.4).

4.3.2 OM pores and IM pores

At present, it is difficult to exactly determine the OM and IM pores of shales (Löhr et al., 2015; Gu et al., 2016). For the studied shales under dried conditions, the TOC contents exhibit remarkably positive linear correlations with the pore surfaces and volumes of the micropores and total pores (Figs. 5(a), 5(c), 5(d), 5(f)); thus, the OM and IM pore surfaces and volumes of the micropores (i.e., $S_{\text{mic-OM}}$ and $V_{\text{mic-OM}}$, $S_{\text{mic-IM}}$ and $V_{\text{mic-IM}}$) and total pores (i.e., $S_{\text{total-OM}}$ and $V_{\text{total-OM}}$, $S_{\text{total-IM}}$ and $V_{\text{total-IM}}$) can be approximately calculated by the linear regression method as described by Cheng et al. (2018). Then, the OM and IM pore surfaces and volumes of the non-micropores (i.e., $S_{\text{non-OM}}$ and $V_{\text{non-OM}}$, $S_{\text{non-IM}}$ and $V_{\text{non-IM}}$) can be obtained by subtracting the calculated micropore surfaces and volumes from the calculated total pore surfaces and volumes.

The calculated OM and IM pore surfaces and volumes

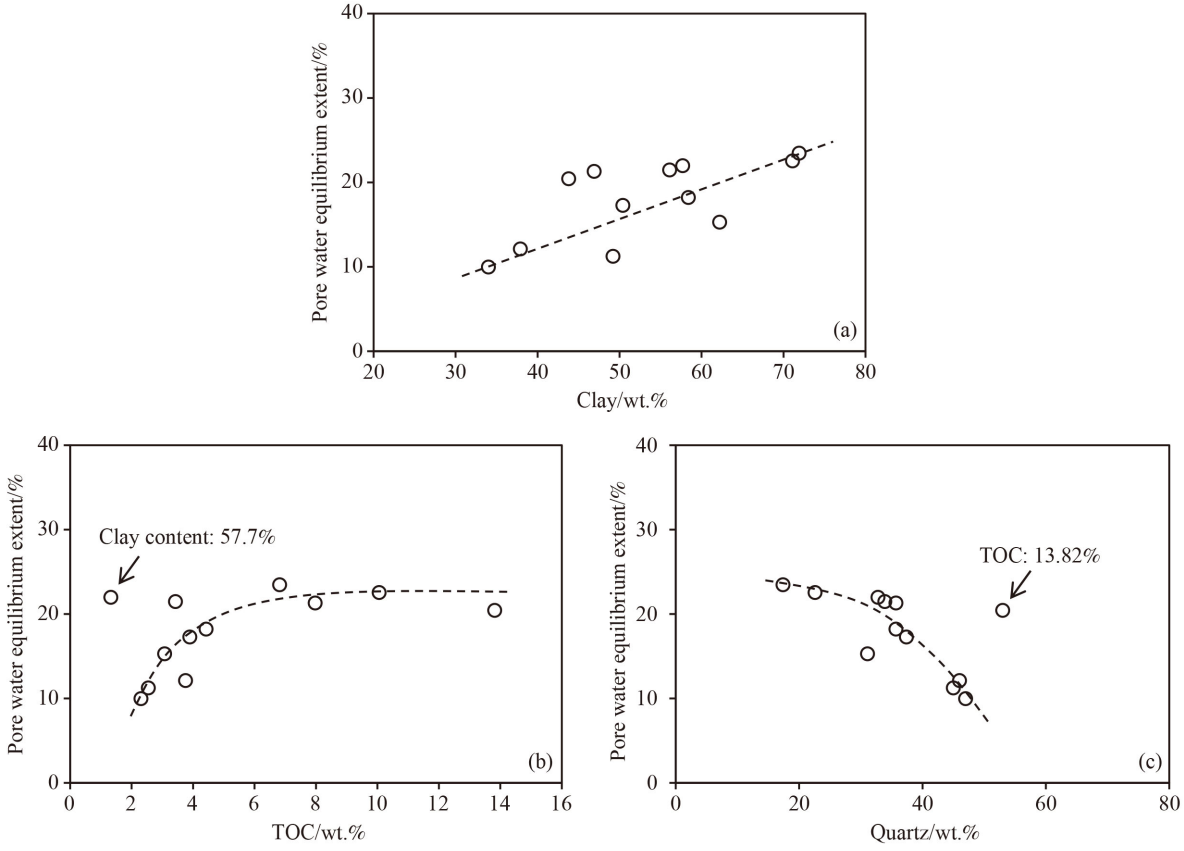

Fig. 4 Correlations of the pore water equilibrium extents with the clay (a), TOC (b), and quartz contents (c) for the studied coal-measure shales.

Table 3 Pore structure parameters of the studied coal-measure shales under both as-received and dried conditions

Sample No.	Depth/m	Formation	Dry condition						As-received condition					
			Micropore		Non-micropore		Total pore		Micropore		Non-micropore		Total pore	
			S_{mic} / ($m^2 \cdot g^{-1}$)	V_{mic} / ($cm^3 \cdot g^{-1}$)	$S_{non\text{-}mic}$ / ($m^2 \cdot g^{-1}$)	$V_{non\text{-}mic}$ / ($cm^3 \cdot g^{-1}$)	S_{total} / ($m^2 \cdot g^{-1}$)	V_{total} / ($cm^3 \cdot g^{-1}$)	S_{mic} / ($m^2 \cdot g^{-1}$)	V_{mic} / ($cm^3 \cdot g^{-1}$)	$S_{non\text{-}mic}$ / ($m^2 \cdot g^{-1}$)	$V_{non\text{-}mic}$ / ($cm^3 \cdot g^{-1}$)	S_{total} / ($m^2 \cdot g^{-1}$)	V_{total} / ($cm^3 \cdot g^{-1}$)
WXN22-1	1880.56	Shanxi	12.36	0.0056	4.04	0.0129	16.41	0.0185	7.60	0.0028	1.08	0.0071	8.68	0.0098
WXN22-2	1891.29	Shanxi	13.71	0.0057	3.75	0.0133	17.46	0.0190	8.81	0.0034	1.03	0.0067	9.84	0.0101
WXN22-3	1901.1	Shanxi	41.59	0.0167	7.80	0.0214	49.39	0.0381	24.50	0.0113	0.91	0.0054	25.41	0.0167
WXN22-4	1910.06	Shanxi	19.06	0.0078	5.13	0.0150	24.19	0.0228	9.91	0.0039	0.94	0.0055	10.85	0.0093
WXN22-5	1922.07	Shanxi	17.09	0.0070	6.15	0.0153	23.25	0.0222	9.47	0.0036	1.05	0.0064	10.52	0.0100
WXN22-6	1930.44	Shanxi	19.21	0.0079	4.57	0.0149	23.78	0.0229	12.92	0.0050	1.06	0.0073	13.98	0.0123
WXN22-7	1933.2	Shanxi	35.80	0.0141	6.63	0.0153	42.42	0.0294	23.33	0.0094	0.86	0.0050	24.19	0.0144
WXN22-8	1939.67	Shanxi	17.08	0.0070	4.85	0.0161	21.93	0.0231	7.65	0.0029	1.24	0.0072	8.89	0.0100
WXN22-9	1967.09	Taiyuan	62.05	0.0244	8.60	0.0260	70.65	0.0504	41.40	0.0174	0.93	0.0051	42.32	0.0225
WXN22-10	1971.89	Taiyuan	13.59	0.0057	6.21	0.0096	19.80	0.0153	7.10	0.0028	0.94	0.0058	8.05	0.0085
WXN22-11	1986.64	Taiyuan	20.41	0.0084	6.44	0.0139	26.84	0.0223	10.29	0.0041	0.91	0.0057	11.19	0.0098
WXN22-12	2010.53	Taiyuan	32.16	0.0129	6.04	0.0133	38.21	0.0262	16.37	0.0082	0.79	0.0046	17.16	0.0127

of the studied shales are presented in Table 4 and Fig. 7, and a brief discussion is provided in this study that is based on each average pore structure parameter value. The micropore structures of shales are mainly contributed by the OM pores, while the non-micropore structures are mainly provided by the IM pores (Fig. 7). Additionally, the S_{total} values of the shales are dominated by the OM pores, except for sample WXN22-10 (Fig. 7(c)), while

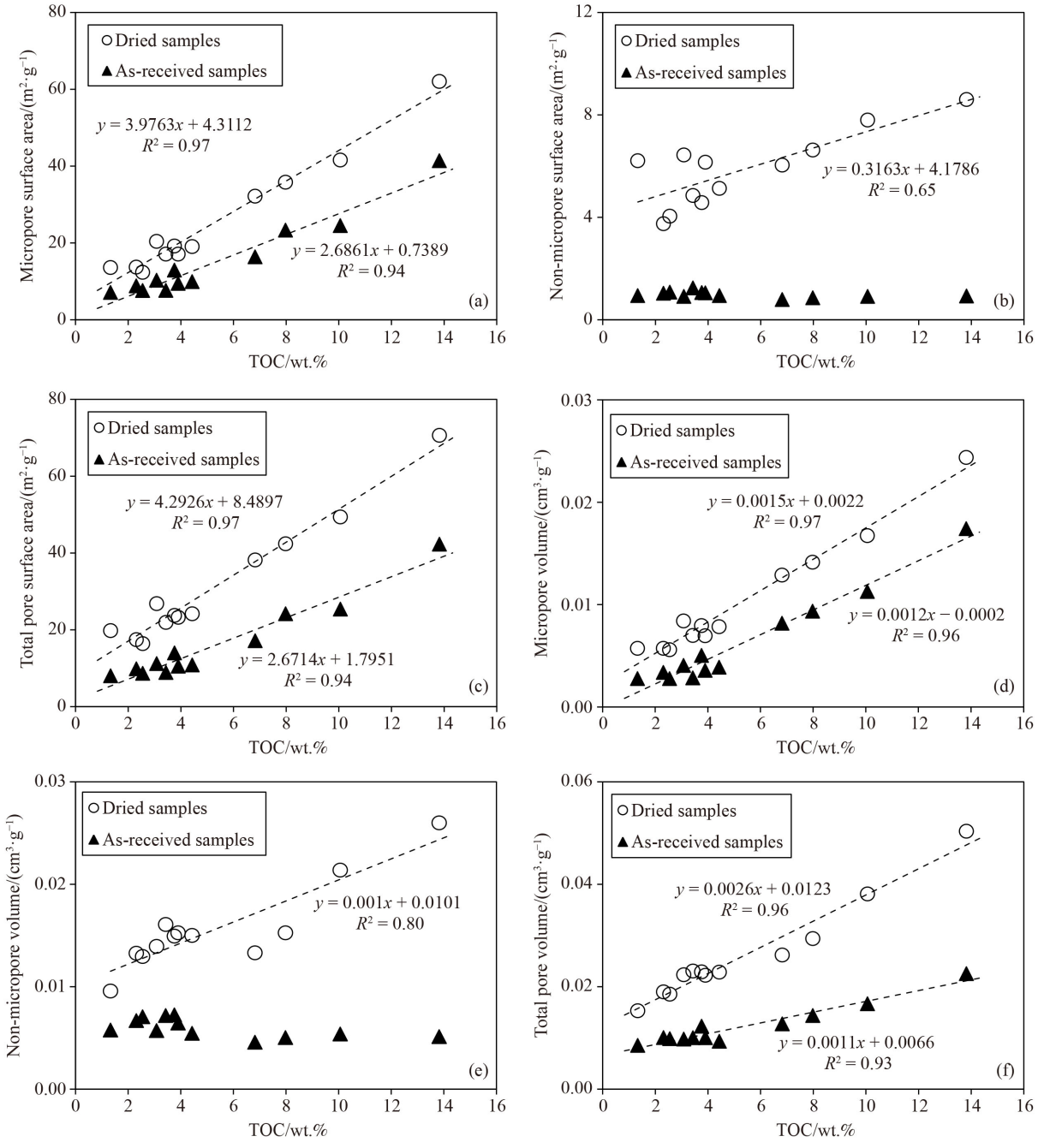

Fig. 5 Correlations of the surface areas and volumes of micropore (a, d), non-micropore (b, e) and total pore (c, f) with the TOC contents for the studied coal-measure shales under both dried and as-received conditions.

the V_{total} values of the shales are mainly contributed by the IM pores for shales with TOC contents < 4 wt.% and by both IM and OM pores for shales with TOC contents > 4 wt.% (Fig. 7(f)). Combined with the pore structure data of the studied shales mentioned in Section 4.3.1, it can be further deduced that the S_{total} values of the studied shales are dominantly derived from $S_{mic\text{-}OM}$, and the V_{total} values of the shales are mainly contributed by $V_{non\text{-}IM}$ as well as $V_{mic\text{-}OM}$.

4.4 Effects of pore water on shale nanopores

4.4.1 Effects of pore water on the micropores and non-micropores

In this study, the water-occupied pore surfaces and volumes of the as-received shale samples and their percentages (P_W) in these pore structures of the dried shale samples (Table 5) are used to reveal the effects of pore water on various shale nanopores. The results

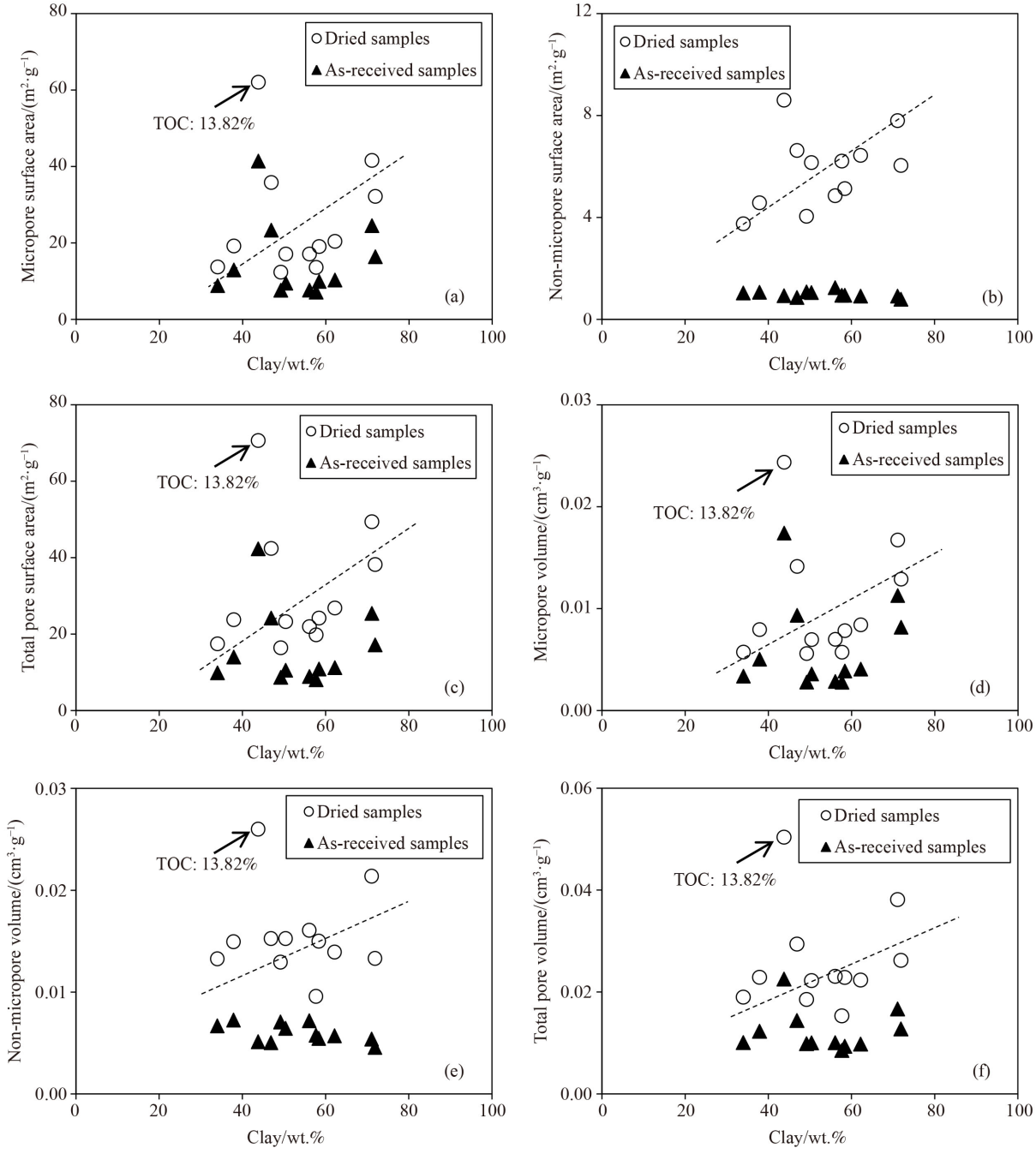

Fig. 6 Correlations of the surface areas and volumes of micropore (a, d), non-micropore (b, e) and total pore (c, f) with the clay contents for the studied coal-measure shales under both dried and as-received conditions.

indicate that, except for samples WXN22-9 and WXN22-10, the water-occupied pore surfaces and volumes of the other shales exhibit remarkably positive correlations with the pore water contents, with correlation coefficients (R^2) ranging from 0.69 to 0.92 (Fig. 8). In addition, the effects of pore water on non-micropores are more significant than those on micropores. Meanwhile, the extents of influence of the pore water are similar on S_{mic} and V_{mic} but are greater on S_{non} than on V_{non} (Table 5), which indicates that the pore water may fill the micropores in a condensed state while occupying the non-micropore surface areas in an absorbed state (Cheng et al., 2017).

Although the studied coal-measure shales have pore water contents that are similar to those of the marine shales reported by Sun et al. (2020a), the pore water has greater effects on the pore structures of the coal-measure shales than on those of the marine shales. For example, the average P_W values of S_{non} and V_{mic} are 81.99% and 43.44% for the studied shales (Table 6), respectively, while they are 61% and 30% for marine shales,

Table 4 Calculated OM and IM pore structure parameters of the studied coal-measure shales under dried conditions

Sample No.	Depth/m	Formation	Pore surface area/($m^2 \cdot g^{-1}$)						Pore volume/($cm^3 \cdot g^{-1}$)					
			Micropore		Non-micropore		Total pore		Micropore		Non-micropore		Total pore	
			$S_{mic\text{-}OM}$	$S_{mic\text{-}IM}$	$S_{non\text{-}OM}$	$S_{non\text{-}IM}$	$S_{total\text{-}OM}$	$S_{total\text{-}IM}$	$V_{mic\text{-}OM}$	$V_{mic\text{-}IM}$	$V_{non\text{-}OM}$	$V_{non\text{-}IM}$	$V_{total\text{-}OM}$	$V_{total\text{-}IM}$
WXN22-1	1880.56	Shanxi	10.14	2.22	0.81	3.24	10.95	5.46	0.0038	0.0018	0.0028	0.0101	0.0066	0.0119
WXN22-2	1891.29	Shanxi	9.19	4.53	0.73	3.02	9.92	7.55	0.0035	0.0023	0.0025	0.0107	0.0060	0.0130
WXN22-3	1901.1	Shanxi	40.00	1.59	3.18	4.62	43.18	6.20	0.0151	0.0016	0.0111	0.0103	0.0262	0.0120
WXN22-4	1910.06	Shanxi	17.62	1.44	1.40	3.73	19.02	5.17	0.0066	0.0012	0.0049	0.0101	0.0115	0.0113
WXN22-5	1922.07	Shanxi	15.51	1.59	1.23	4.92	16.74	6.50	0.0059	0.0011	0.0043	0.0110	0.0101	0.0121
WXN22-6	1930.44	Shanxi	14.95	4.25	1.19	3.38	16.14	7.64	0.0056	0.0023	0.0041	0.0108	0.0098	0.0131
WXN22-7	1933.2	Shanxi	31.73	4.07	2.52	4.10	34.25	8.17	0.0120	0.0022	0.0088	0.0065	0.0207	0.0087
WXN22-8	1939.67	Shanxi	13.64	3.44	1.08	3.77	14.72	7.21	0.0051	0.0019	0.0038	0.0123	0.0089	0.0142
WXN22-9	1967.09	Taiyuan	54.95	7.10	4.37	4.23	59.32	11.33	0.0207	0.0036	0.0152	0.0108	0.0359	0.0144
WXN22-10	1971.89	Taiyuan	5.29	8.30	0.42	5.79	5.71	14.09	0.0020	0.0037	0.0015	0.0081	0.0035	0.0119
WXN22-11	1986.64	Taiyuan	12.25	8.16	0.97	5.46	13.22	13.62	0.0046	0.0038	0.0034	0.0105	0.0080	0.0143
WXN22-12	2010.53	Taiyuan	27.12	5.04	2.16	3.89	29.28	8.93	0.0102	0.0027	0.0075	0.0058	0.0177	0.0085

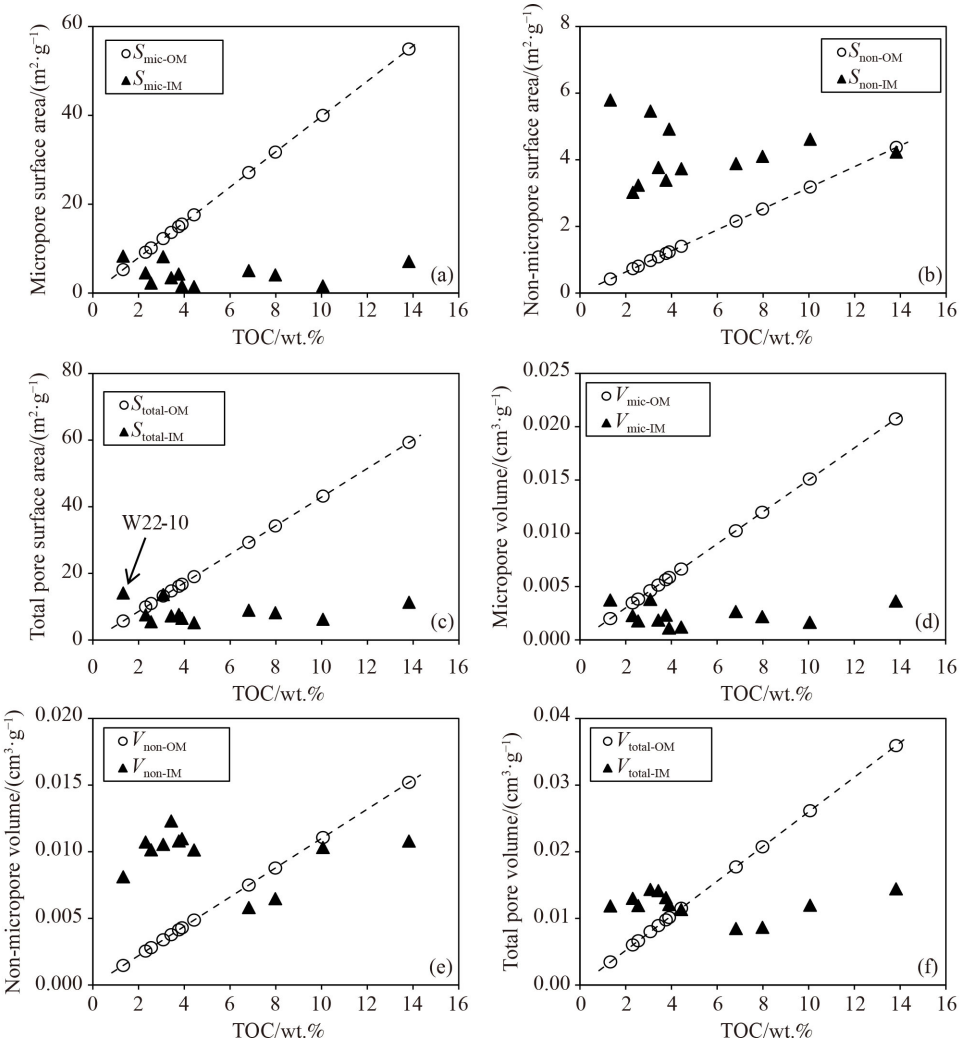

Fig. 7 Correlations of the OM and IM pore surfaces and volumes of micropore (a, d), non-micropore (c, e) and total pore (c, f) with the TOC contents for the studied coal-measure shales.

Table 5 Calculated water-occupied pore structures of the as-received shale samples and their percentages (P_W) in the pore structures of the dried shale samples

Sample No.	Water-occupied pore surface area/($m^2 \cdot g^{-1}$)								
	Micropore			Non-micropore			Total pore		
	$S_{mic\text{-}OMW}$	$S_{mic\text{-}IMW}$	$S_{mic\text{-}W}$	$S_{non\text{-}OMW}$	$S_{non\text{-}IMW}$	$S_{non\text{-}W}$	$S_{total\text{-}OMW}$	$S_{total\text{-}IMW}$	$S_{total\text{-}W}$
WXN22-1	2.53 (25.0%) [a)]	2.22 (100.0%)	4.76 (38.5%)	0.00 (0.0%)	2.97 (91.7%)	2.97 (73.4%)	2.53 (23.2%)	5.19 (95.1%)	7.73 (47.1%)
WXN22-2	0.35 (4.1%)	4.53 (100.0%)	4.90 (35.8%)	0.00 (0.0%)	2.72 (90.0%)	2.72 (72.5%)	0.38 (3.8%)	7.25 (96.0%)	7.62 (43.7%)
WXN22-3	15.50 (38.8%)	1.59 (100.0%)	17.09 (41.1%)	2.27 (71.3%)	4.62 (100.0%)	6.89 (88.3%)	17.77 (41.2%)	6.20 (100.0%)	23.97 (48.5%)
WXN22-4	7.71 (43.7%)	1.44 (100.0%)	9.15 (48.0%)	0.46 (32.7%)	3.73 (100.0%)	4.19 (81.6%)	8.16 (42.9%)	5.17 (100.0%)	13.34 (55.1%)
WXN22-5	6.04 (38.9%)	1.59 (100.0%)	7.62 (44.6%)	0.18 (14.8%)	4.92 (100.0%)	5.10 (82.9%)	6.22 (37.1%)	6.50 (100.0%)	12.72 (54.7%)
WXN22-6	2.03 (13.6%)	4.25 (100.0%)	6.29 (32.7%)	0.13 (10.9%)	3.38 (100.0%)	3.51 (76.8%)	2.16 (13.4%)	7.64 (100.0%)	9.80 (41.2%)
WXN22-7	8.40 (26.5%)	4.07 (100.0%)	12.47 (34.8%)	1.67 (66.1%)	4.10 (100.0%)	5.77 (87.1%)	10.07 (29.4%)	8.17 (100.0%)	18.24 (43.0%)
WXN22-8	5.99 (43.9%)	3.44 (100.0%)	9.43 (55.2%)	0.00 (0.0%)	3.61 (95.8%)	3.61 (74.4%)	5.99 (40.7%)	7.05 (97.8%)	13.04 (59.5%)
WXN22-9	13.56 (24.7%)	7.10 (100.0%)	20.66 (33.3%)	3.45 (78.8%)	4.23 (100.0%)	7.67 (89.0%)	17.00 (28.7%)	11.33 (100.0%)	28.33 (40.1%)
WXN22-10	0.00 (0.0%)	6.48 (78.1%)	6.48 (47.7%)	0.00 (0.0%)	5.27 (91.0%)	5.27 (84.8%)	0.00 (0.0%)	11.75 (83.4%)	11.75 (59.4%)
WXN22-11	1.96 (16.0%)	8.16 (100.0%)	10.12 (49.6%)	0.07 (6.7%)	5.46 (100.0%)	5.53 (85.9%)	2.03 (15.3%)	13.62 (100.0%)	15.65 (58.3%)
WXN22-12	10.74 (39.6%)	5.04 (100.0%)	15.79 (49.1%)	1.37 (63.4%)	3.89 (100.0%)	5.25 (86.9%)	12.11 (41.4%)	8.93 (100.0%)	21.04 (55.1%)

Sample No.	Water-occupied pore volume/($cm^3 \cdot g^{-1}$)								
	Micropore			Non-micropore			Total pore		
	$V_{mic\text{-}OMW}$	$V_{mic\text{-}IMW}$	$V_{mic\text{-}W}$	$V_{non\text{-}OMW}$	$V_{non\text{-}IMW}$	$V_{non\text{-}W}$	$V_{total\text{-}OMW}$	$V_{total\text{-}IMW}$	$V_{total\text{-}W}$
WXN22-1	0.0010 (27.2%)	0.0018 (100.0%)	0.0028 (50.3%)	0.0000 (0.0%)	0.0059 (58.0%)	0.0059 (45.5%)	0.0010 (15.7%)	0.0077 (64.3%)	0.0087 (46.9%)
WXN22-2	0.0001 (2.5%)	0.0023 (100.0%)	0.0024 (41.1%)	0.0000 (0.0%)	0.0066 (61.4%)	0.0066 (49.6%)	0.0001 (1.4%)	0.0089 (68.1%)	0.0089 (47.0%)
WXN22-3	0.0038 (25.2%)	0.0016 (100.0%)	0.0055 (32.6%)	0.0057 (51.4%)	0.0103 (100.0%)	0.0160 (74.8%)	0.0095 (36.3%)	0.0120 (100.0%)	0.0215 (56.3%)
WXN22-4	0.0028 (41.6%)	0.0012 (100.0%)	0.0040 (50.5%)	0.0000 (0.0%)	0.0096 (94.3%)	0.0096 (63.7%)	0.0028 (24.0%)	0.00108 (94.9%)	0.0135 (59.1%)
WXN22-5	0.0023 (38.8%)	0.0011 (100.0%)	0.0034 (48.5%)	0.0000 (0.0%)	0.0088 (80.4%)	0.0088 (57.8%)	0.0023 (22.4%)	0.0099 (82.2%)	0.0122 (54.9%)
WXN22-6	0.0006 (10.8%)	0.0023 (100.0%)	0.0029 (36.7%)	0.0000 (0.0%)	0.0077 (71.1%)	0.0077 (51.4%)	0.0006 (6.2%)	0.0100 (76.2%)	0.0106 (46.3%)
WXN22-7	0.0026 (21.9%)	0.0022 (100.0%)	0.0048 (33.9%)	0.0037 (42.7%)	0.0065 (100.0%)	0.0102 (67.0%)	0.0064 (30.7%)	0.0087 (100.0%)	0.0150 (51.1%)
WXN22-8	0.0023 (44.6%)	0.0019 (100.0%)	0.0041 (59.3%)	0.0000 (0.0%)	0.0089 (72.3%)	0.0089 (55.3%)	0.0023 (25.7%)	0.0107 (75.9%)	0.0130 (56.5%)
WXN22-9	0.0033 (16.0%)	0.0036 (100.0%)	0.0070 (28.5%)	0.0101 (66.3%)	0.0108 (100.0%)	0.0209 (80.3%)	0.0134 (37.3%)	0.0144 (100.0%)	0.0278 (55.2%)
WXN22-10	0.0000 (0.0%)	0.0030 (79.1%)	0.0030 (51.6%)	0.0000 (0.0%)	0.0038 (47.0%)	0.0038 (39.9%)	0.0000 (0.0%)	0.0068 (57.1%)	0.0068 (44.2%)
WXN22-11	0.0006 (12.1%)	0.0038 (100.0%)	0.0044 (51.7%)	0.0000 (0.0%)	0.0082 (78.0%)	0.0082 (59.0%)	0.0006 (7.0%)	0.0120 (83.8%)	0.0126 (56.3%)
WXN22-12	0.0021 (20.1%)	0.0027 (100.0%)	0.0047 (36.6%)	0.0029 (39.0%)	0.0058 (100.0%)	0.0087 (65.6%)	0.0050 (28.1%)	0.0085 (100.0%)	0.0135 (51.3%)

Note: [a)] The data in the brackets are the P_W values for each water-occupied pore structure.

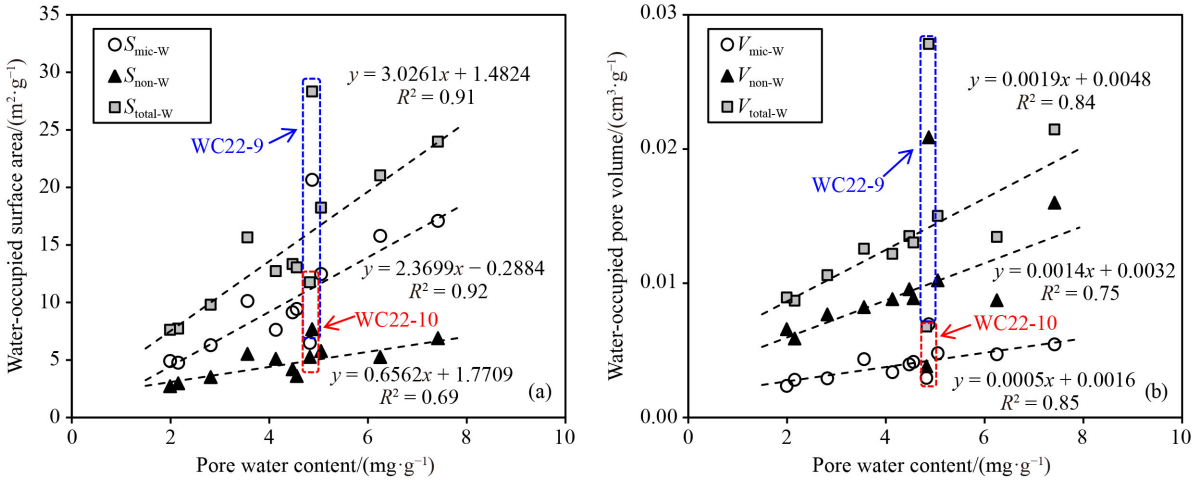

Fig. 8 Correlations of the water-occupied pore surface areas (a) and volumes (b) with the pore water contents for the studied shales. The water-occupied pore surfaces and volumes of shales exhibit linear positive correlations with the C_{PW} values, except for samples WXN22-9 and WXN22-10.

Table 6 Average percentages of each water-occupied pore surface and volumes of the studied shales under as-received conditions in the pore structure of the shales under dried conditions

Pore structures	Average water-occupied percentage of pore structures/(P_W, %)					
	Pore volume			Pore surface area		
	OM pore	IM pore	OM + IM pore [a)]	OM pore	IM pore	OM + IM pore
Micropore	26.23	98.18	42.53	21.74	98.26	43.44
Non-micropore	28.73	97.37	81.99	16.61	80.2	59.16
Total pore	26.42	97.69	50.47	19.57	83.54	52.11

Note: [a)] Sum of the organic-matter hosted (OM) and inorganic-matter hosted (IM) pore structures.

respectively (Sun et al., 2020a). This is probably because the coal-measure shales are characterized by high clay contents and type III kerogen, which result in the studied shales having a stronger capacity to hold water than the marine shales (Gu et al., 2016; Gao et al., 2019).

The low-pressure gas adsorption isotherms and pore size distributions (PSDs) of V_{mic} and S_{non} for samples WXN22-2, WXN22-3, and WXN22-4 were used to further demonstrate the effects of pore water on nanopores with diverse pore widths (Figs. 9 and 10). With successive increases in the TOC and clay contents of samples WXN22-2, WXN22-4, and WXN22-3 (Table 1), the differences in the CO_2 and N_2 adsorption isotherms between the dried and as-received shale samples progressively increase (Figs. 9 and 10), which is consistent with the increases in their pore water contents (Table 2). The micropore PSDs of all three samples show that micropores with pore widths < 0.5 nm were not detected in the as-received samples (Figs. 9(d), 9(e), 9(f)), which indicates that these micropores may be fully blocked or occupied by pore water. Li et al. (2017) also reported that pore water can totally take up or block the IM pores of shales with pore widths < 0.6–0.7 nm. The N_2 gas adsorption and desorption isotherms show obvious hysteresis loops for the dried shales, while the hysteresis loops are absent for the as-received shales (Figs. 10(a), 10(b), 10(c)). This implies that shales contain narrow pore network systems that induce pore retention effects; however, under as-received conditions, pore water may condense or form water films on the pore mouth of pores with narrow pore widths and block these pores, which obviously decreases the pore retention effects (Thommes et al., 2015; Bertier et al., 2016; Lahn et al., 2020). In addition, compared with the non-micropores with pore widths > 8 nm, the non-micropores with pore widths < 8 nm are occupied by pore water more significantly (Figs. 10(d), 10(e), 10(f)), which probably occurs because the former non-micropores have stronger capillary binding forces than the latter non-micropores (Wu et al., 2017).

4.4.2 Effects of pore water on OM and IM pores

Because the hydrophilicity of the IM pores is higher than that of the OM pores when the two types of pores have similar pore widths (McCutcheon and Barton, 1999; Gu et al., 2016; Cheng et al., 2018), under certain geological conditions, the pore water may preferentially take up the IM pores of shales, and after the IM pores are fully

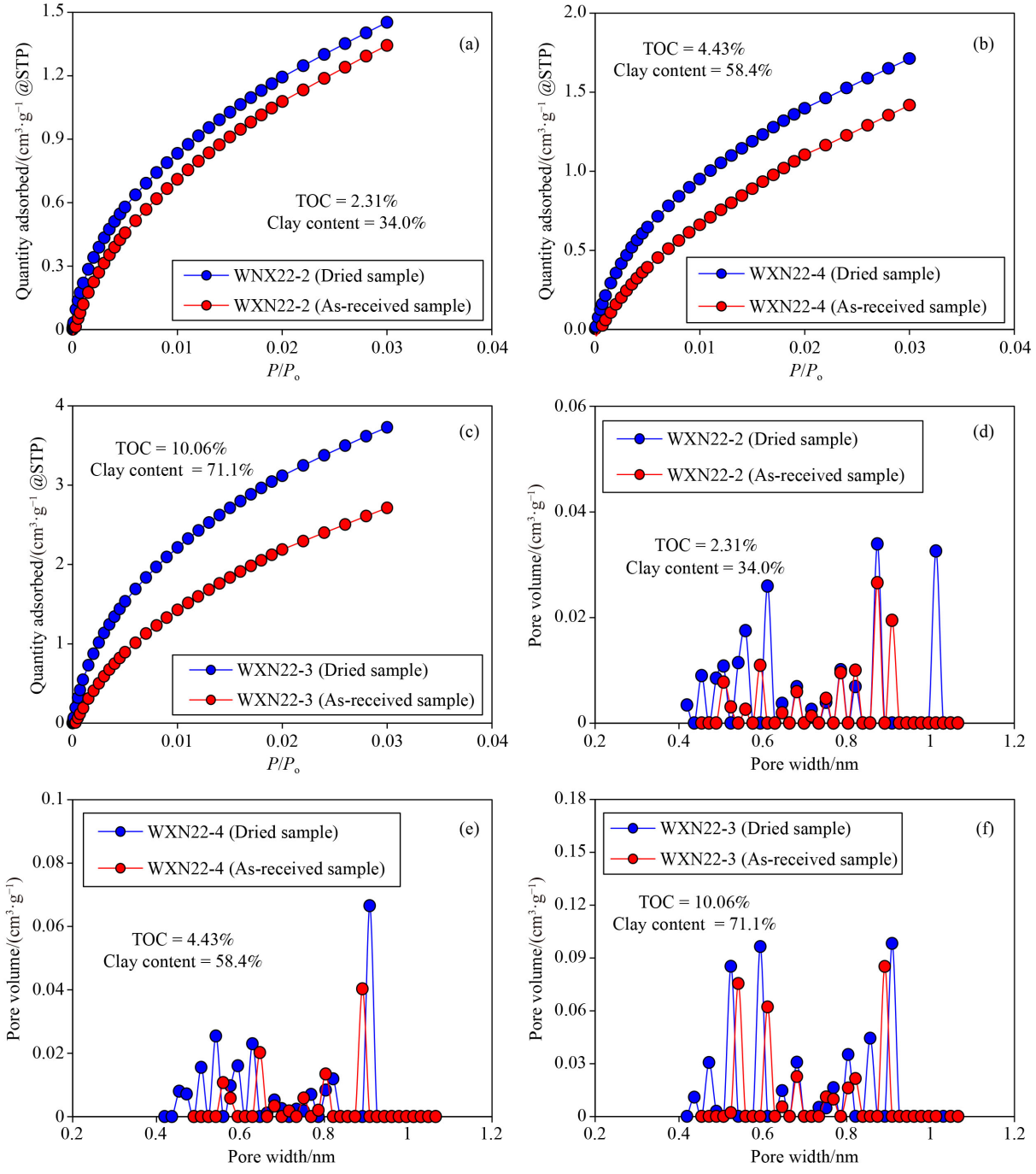

Fig. 9 The low-pressure CO_2 adsorption isotherms (a, b, c) and the micropore pore volume distributions (d, e, f) of three selected shale samples under both dried and as-received conditions.

occupied, the excess water would then occupy the OM pores. Therefore, if the water-occupied pore surface and volumes of the shales are smaller than their IM pore structures, this implies that the pore water only takes up part of the IM pores but none of the OM pores of shales. However, if the water-occupied pore surfaces and volumes of the shales are greater than their IM pore structures, this implies that pore water occupies all of the IM pore surfaces and volumes as well as a portion of the OM pore structures of the shales.

Based on the above assumptions, this study approximately evaluates the effects of pore water on the IM and OM pore structures of shales. The results show that the average water-occupied surface areas of the OM micropores ($S_{mic\text{-}OMW}$), non-micropores ($S_{non\text{-}OMW}$), and total pores ($S_{total\text{-}OMW}$) are 6.24 m^2/g, 0.80 m^2/g, and 7.04 m^2/g, respectively, and that their P_w values are 26.23%, 28.73%, and 26.42%, respectively (Table 5 and Table 6). The $S_{mic\text{-}OMW}$ values are much higher than the $S_{non\text{-}OMW}$ values, but the P_w values are similar (Fig. 11).

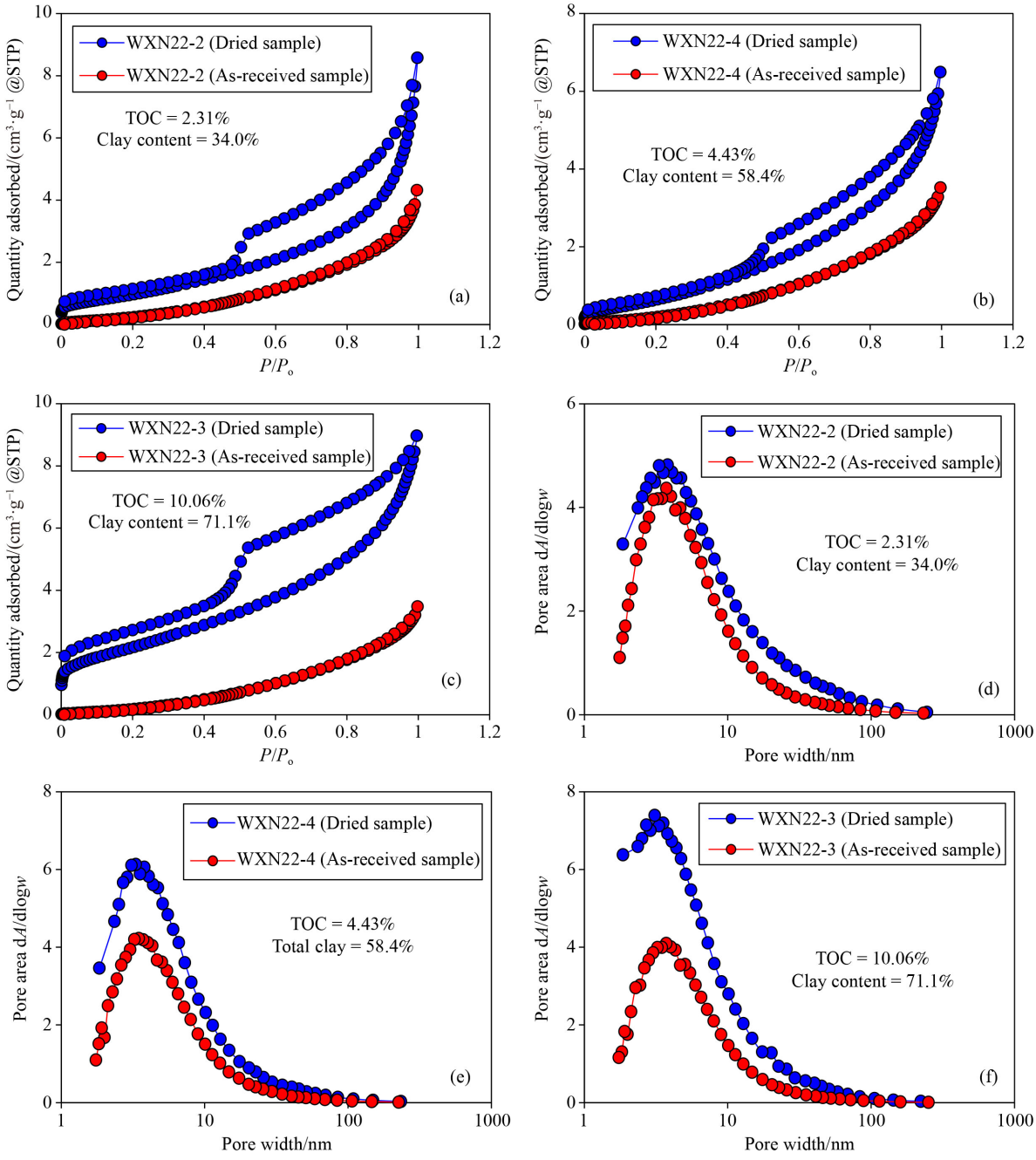

Fig. 10 The low-pressure N_2 adsorption and desorption isotherms (a, b, c) and the non-micropore pore surface area distributions (d, e, f) of three selected shale samples under both dried and as-received conditions.

The average water-occupied surface areas of the IM micropores ($S_{mic\text{-}IMW}$), non-micropores ($S_{non\text{-}IMW}$) and total pores ($S_{total\text{-}IMW}$) are 4.16 m^2/g, 4.07 m^2/g, and 8.23 m^2/g, respectively, and their P_w values are 98.18%, 97.37%, and 97.69%, respectively (Table 5 and Table 6). The $S_{mic\text{-}IMW}$ and $S_{non\text{-}IMW}$ values as well as their P_w values are similar (Fig. 11). The average water-occupied pore volumes of the OM micropores ($V_{mic\text{-}OMW}$), non-micropores ($V_{non\text{-}OMW}$), and total pores ($V_{total\text{-}OMW}$) are 0.0018 cm^3/g, 0.0019 cm^3/g, and 0.0037 cm^3/g, respectively, and their P_w values are 21.74%, 16.61%, and 19.57%, respectively (Table 5 and Table 6). The $V_{mic\text{-}OMW}$ values are similar to the $V_{non\text{-}OMW}$ values, but the P_w values of the former are greater than those of the latter (Fig. 11). The average water-occupied pore volumes of the IM micropores ($V_{mic\text{-}IMW}$), non-micropores ($V_{non\text{-}IMW}$), and total pores ($V_{total\text{-}IMW}$) are 0.0023 cm^3/g, 0.0077 cm^3/g, and 0.0100 cm^3/g, respectively, and their P_w values are 98.26%, 80.20%, and 83.54%, respectively (Table 5 and Table 6). The $V_{mic\text{-}IMW}$ values are much smaller than the $V_{non\text{-}IMW}$ values, but the P_w values of the former are greater than those of the latter (Fig. 11). Therefore, the

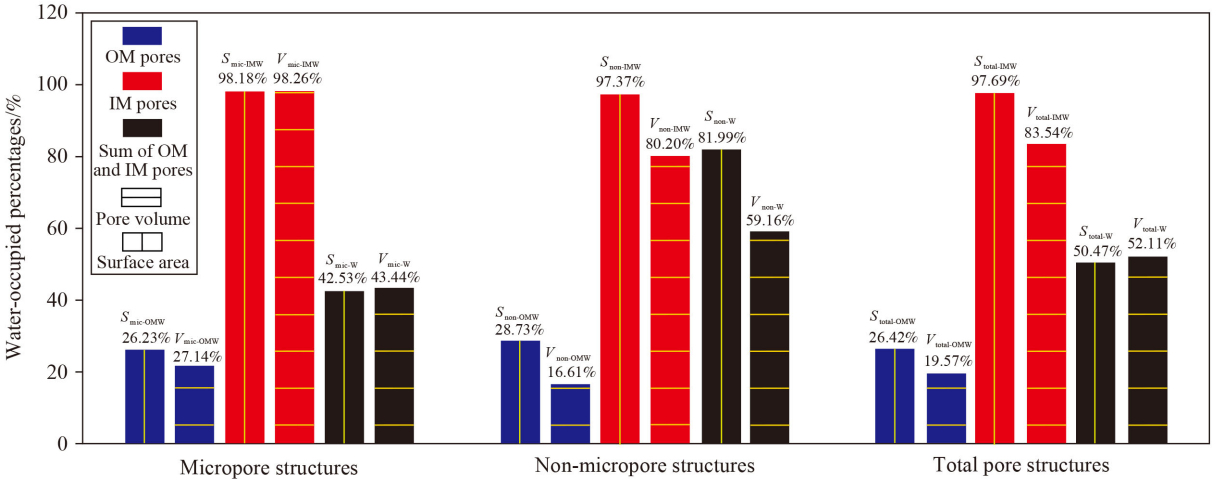

Fig. 11 Percentages of each water-occupied pore structure of the shales under as-received conditions in the pore structures of the shales under dried conditions (P_W). The P_W values show that the effects of pore water on shale nanopores with various types and pore widths are different.

effects of pore water are more significant on the IM pore structures than on the OM pore structures for either the micropores or non-micropores of the studied coal-measure shales.

4.5 Implications for shale gas storage

Although pore water significantly occupies the pore surface and volumes of coal-measure shales, a certain amount of effective pore structures remains for the storage of shale gas. The effective pore spaces in the studied shales can be estimated by the differences between the pore spaces of the dried shales (Table 4) and the water-occupied pore spaces of the as-received shales (Table 5). The average percentages of each effective pore structure (P_E) for the studied shales are listed in Table 7. The P_E values for S_{mic-OM}, S_{non-OM}, S_{mic-IM}, and S_{non-IM} are 44.90%, 3.31%, 0.76%, and 0.56%, respectively, with a total of 49.53%. The P_E values for V_{mic-OM}, V_{non-OM}, V_{mic-IM}, and V_{non-IM} are 21.55%, 15.59%, 0.43%, and 10.32%, respectively, with a total of 47.89% (Table 7 and Fig. 12). These data indicate that approximately half of the total pore spaces of the as-received shales are available for the storage of shale gas, and most of the effective pore spaces are provided by the OM pores.

Although overmature gas shales underwent strong displacement drainages during thermal evolution stages (Wardlaw and McKellar, 1998; Mahadevan et al., 2007; Cheng et al., 2019), these shales still retained certain amounts of pore water (Bennion and Thomas, 2005; Liu and Wang, 2013; Fang et al., 2014; Cheng et al., 2018). The pore water can significantly influence the gas-bearing properties of shales; it not only reduces the gas-in-place (GIP) contents by occupying many effective pore spaces for shale gas but also causes the shale gas, especially the absorbed gas, to be mostly stored in the OM pores of shales, while the IM pores mainly store free gas. In addition, although the coal-measure shales in the Qinshui

Table 7 Average percentage, water-occupied percentage and effective percentage of each pore structure in the total pore structure of the studied coal-measure shales under both dried and as-received conditions

Pore structures		Average percentage in total pore structure/%		
		Shales under dried conditions	Shales under as-received conditions	
		Relative percentage	Water-occupied percentage	Effective percentage
Surface area	S_{mic-OM}	62.99	18.09	44.90
	S_{mic-IM}	16.18	15.42	0.76
	S_{non-OM}	5.01	1.70	3.31
	S_{non-IM}	15.81	15.25	0.56
Pore volume	V_{mic-OM}	27.95	6.40	21.55
	V_{mic-IM}	10.03	9.60	0.43
	V_{non-OM}	20.49	4.90	15.59
	V_{non-IM}	41.52	31.20	10.32

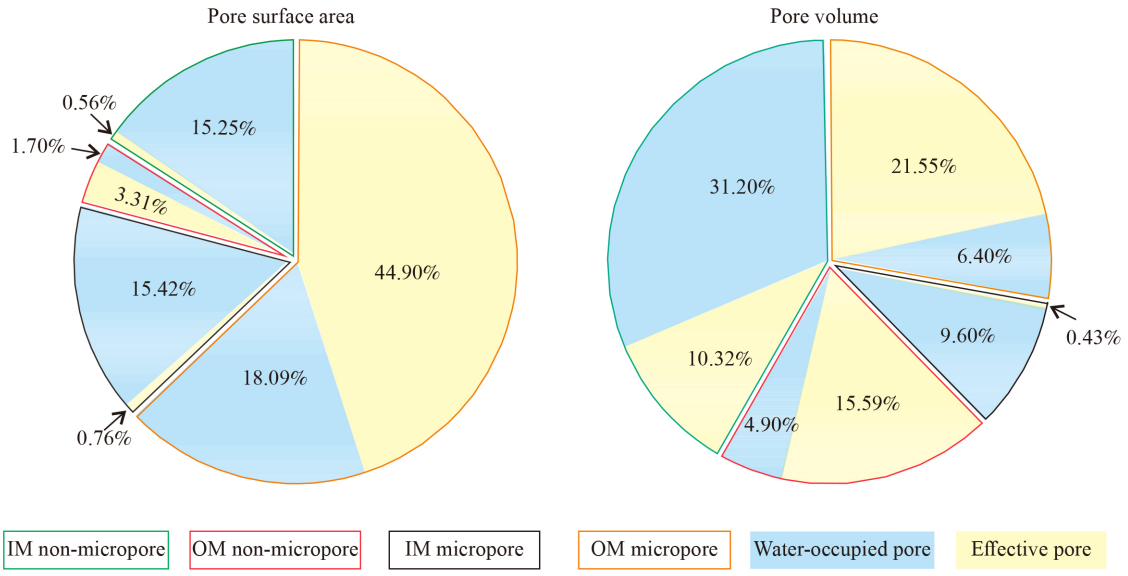

Fig. 12 Water-occupied and effective percentages of each pore structure in the total pore structure of the studied coal-measure shales under as-received conditions, showing that pore water in the shales can significantly influence the effective pore structures for the storage of shale gas.

Basin have similar pore water contents to those of the marine shales from some blocks in the southern China area (Cheng et al., 2018; Sun et al., 2020b), the effects of pore water are more significant on the former shales than on the latter shales because the two types of shales differ in their mineral compositions, organic matter types and nanopore structures. The bulk pore systems of coal-measure shales have greater water-bearing extents than those of marine shales, which results in retaining a smaller proportion of the pore structures to store shale gas. Therefore, the water-bearing characteristics and their effects on the nanopores of overmature coal-measure shales should be highly considered for shale gas exploration and development in the Qinshui Basin.

5 Conclusions

This study investigates the water-bearing characteristics and their effects on the nanopores of coal-measure shales taken from the Qinshui Basin, north China, and mainly reaches the following conclusions.

1) The pore water contents (C_{PW}) of the studied shales are much lower than their equilibrium water contents (C_{EW}), which indicates that the bulk pore systems of the shales have low water-bearing extents, with pore water equilibrium extents (E_{PW}) ranging from 9.98% to 23.47%.

2) The influences of pore water are more significant on the non-micropores and IM pores than on the micropores and OM pores, respectively, for the studied coal-measure shales, especially for the pore surfaces of IM pores.

3) The pore water of coal-measure shales not only takes up approximately half of the total pore surfaces and volumes, which reduces the storage space of shale gas, but also causes the shale gas, especially the absorbed gas, to be mainly stored in the OM pores; meanwhile, the IM pores mainly contain free gas.

Acknowledgments This study was supported by the National Natural Science Foundation of China (Grant Nos. U1810201 and 41925014), the Natural Science Foundation of Guangdong Province (No. 2021A1515011381). This is contribution No.IS-3341 from GIGCAS.

Nomenclature

C_{PW} = pore water content
C_{EW} = equilibrium water content
E_{PW} = pore water equilibrium extent
OM = organic-matter hosted
IM = inorganic-matter hosted
S_{mic} = micropore surface area
V_{mic} = micropore volume
S_{non} = non-micropore surface area
V_{non} = non-micropore volume
S_{total} = total pore surface area
V_{total} = total pore volume
R_o = vitrinite reflectance value
T_{max} = maximum cracking temperature
HI = hydrogen index
OI = oxygen index
XRD = X-ray diffraction
P_W = percentage of water-occupied pore structure
P_E = percentage of effective pore structure

References

Ahmad M, Haghighi M (2013). Water saturation evaluation of

Murteree and Roseneath shale gas reservoirs, Cooper Basin, Australia using wire-line logs, focused ion beam milling and scanning electron microscopy. In: SPE Unconventional Resources Conference and Exhibition-Asia Pacific, November 11−13, Brisbane Australia, SPE-167080-MS

Ambrose R J, Hartman R C, Diaz-Campos M D, Akkutlu I Y, Sondergeld C H (2010). New pore-scale considerations for shale gas in place calculations. In: SPE Unconventional Gas Conference, February 23−25, Pittsburgh, Pennsylvania, USA, SPE-131772-MS

ASTM D1412-07 (2010). Standard test method for equilibrium moisture of coal at 96 to 97 percent relative humidity and 30°C. American Society for Testing and Materials: West Conshohocken, PA: 2010

Bekyarova E, Hanzawa Y, Kaneko K, Silvestre-Albero J, Sepulveda-Escribano A, Rodriguez-Reinoso F, Kasuya D, Yudasaka M, Iijima S (2002). Cluster-mediated filling of water vapor in intratube and interstitial nanospaces of single-wall carbon nanohorns. Chem Phys Lett, 366(5–6): 463–468

Bennion D B, Thomas F B (2005). Formation damage issues impacting the productivity of low permeability, low initial water saturation gas producing formations. J Energy Resour Technol, 127(3): 240–247

Bertier P, Schweinar K, Stanjek H, Ghanizadeh A, Clarkson C R, Busch A, Kampman N, Prinz D, Amann-Hildebrand A, Krooss B M, Pipich V (2016). On the use and abuse of N_2 physisorption for the characterization of the pore structure of shales. In: Schäfer T, Dorhmann R, Greenwell H C, eds. Filling the Gaps from Microscopic Pore Structure to Transport Properties in Shales. CMS Workshop Lectures, volume 21: 151–161

Boyer C, Kieschnick J, Suarez-Rivera R, Lewis R E, Waters G (2006). Producing gas from its source. Oilfield Rev, 18: 36–49

Brunauer S, Emmett P H, Teller E (1938). Adsorption of gases in multimolecular layers. J Am Chem Soc, 60(2): 309–319

Bustin R M, Bustin A M M, Cui X, Ross D J K, Murthy Pathi V S (2008). Impact of shale properties on pore structure and storage characteristics. In: SPE Shale Gas Production Conference, November 2008, Fort Worth, Texas, USA

Cai Y D, Liu D M, Yao Y B, Li J Q, Qiu Y K (2011). Geological controls on prediction of coalbed methane of No. 3 coal seam in Southern Qinshui Basin, north China. Int J Coal Geol, 88(2–3): 101–112

Chalmers G R L, Bustin R M (2008). Lower Cretaceous gas shales in northeastern British Columbia, part I: geological controls on methane sorption capacity. Bull Can Pet Geol, 56(1): 1–21

Chalmers G R, Bustin R M, Powers I M (2009). A pore by any other name would be as small: the importance of meso- and microporosity in shale gas capacity. AAPG, Search Discov: 90090

Charrière D, Behra P (2010). Water sorption on coals. J Colloid Interface Sci, 344(2): 460–467

Chen J, Gai H F, Xiao Q L (2021). Effects of composition and temperature on water sorption in overmature Wufeng-Longmaxi shales. Int J Coal Geol, 234: 103673

Chen Z Y, Song Y, Li Z, Liu S B, Li Y H, Liu G H, Yang W, Wang Q Y, Yang Y D, Gao F L (2019). The occurrence characteristics and removal mechanism of residual water in marine shales: a case study of Wufeng-Longmaxi shale in Changning-Weiyuan area, Sichuan Basin. Fuel, 253: 1056–1070

Cheng P, Tian H, Xiao X M, Gai H F, Li T F, Wang X (2017). Water distribution in overmature organic-rich shales: implications from water adsorption experiments. Energy Fuels, 31(12): 13120–13132

Cheng P, Xiao X M, Tian H, Wang X (2018). Water content and equilibrium saturation and their influencing factors of the Lower Paleozoic overmature organic-rich shales in the Upper Yangtze Region of southern China. Energy Fuels, 32(11): 11452–11466

Cheng P, Xiao X M, Wang X, Sun J, Wei Q (2019). Evolution of water content in organic-rich shales with increasing maturity and its controlling factors: implications from a pyrolysis experiment on a water-saturated shale core sample. Mar Pet Geol, 109: 291–303

Cipolla C L, Lolon E P, Erdle J C, Rubin B (2010). Reservoir modeling in shale-gas reservoirs. SPE Reservoir Evaluation & Engineering, 13(4): 638–653

De Silva P N K, Simons S J R, Stevens P, Philip L M (2015). A comparison of North American shale plays with emerging non-marine shale plays in Australia. Mar Pet Geol, 67: 16–29

Dong D Z, Wang Y M, Li X J, Zou C N, Guan Q Z, Zhang C C, Huang J L, Wang S F, Wang H Y, Liu H L, Bai W H, Liang F, Lin W, Zhao Q, Liu D X, Qiu Z (2016a). Breakthrough and prospect of shale gas exploration and development in China. Nat Gas Ind B, 3(1): 12–26

Dong D Z, Zou C N, Dai J X, Huang S P, Zheng J W, Gong J M, Wang Y M, Li X J, Guan Q Z, Zhang C C, Huang J L, Wang S F, Liu D X, Qiu Z (2016b). Suggestions on the development strategy of shale gas in China. Nat Gas Geosci, 1(6): 413–423

Dubinin M M (1989). Fundamentals of the theory of adsorption in micropores of carbon adsorbents: characteristics of their adsorption properties and microporous structures. Carbon, 27(3): 457–467

Fang Z H, Huang Z L, Wang Q Z, Deng D W, Liu H L (2014). Cause and significance of the ultra-low water saturation in gas-riched shale reservoir. Nat Gas Geosci, 25: 471–475 (in Chinese)

Feng D, Li X F, Wang X Z, Li J, Sun F R, Sun Z, Zhang T, Li P H, Chen Y, Zhang X (2018). Water adsorption and its impact on the pore structure characteristics of shale clay. Appl Clay Sci, 155: 126–138

Gao Z Y, Fan Y P, Hu Q H, Jiang Z X, Cheng Y, Xuan Q X (2019). A review of shale wettability characterization using spontaneous imbibition experiments. Mar Pet Geol, 109: 330–338

Gasparik M, Bertier P, Gensterblum Y, Ghanizadeh A, Krooss B M, Littke R (2014). Geological controls on the methane storage capacity in organic-rich shales. Int J Coal Geol, 123: 34–51

Gensterblum Y, Merkel A, Busch A, Krooss B M (2013). High-pressure CH_4 and CO_2 sorption isotherms as a function of coal maturity and the influence of moisture. Int J Coal Geol, 118: 45–57

Gu X, Mildner D F R, Cole D R, Rother G, Slingerland R, Brantley S L (2016). Quantification of organic porosity and water accessibility in Marcellus shale using neutron scattering. Energy Fuels, 30(6): 4438–4449

Guo T L (2016). Key geological issues and main controls on accumulation and enrichment of Chinese shale gas. Pet Explor Dev, 43(3): 349–359

Handwerger D A, Suarez-Rivera R, Vaughn K I, Keller J F (2011). Improved petrophysical core measurements on tight shale reservoirs

using retort and crushed samples. In: SPE Annual Technical Conference and Exhibition, October 2011, Denver, Colorado, USA

Hartman R C, Lasswell P, Bhatta N (2008). Recent advances in the analytical methods used for shale gas reservoir gas-in-place assessment. In: AAPG Annual Convention: San Antonio, TX

Hu Y N, Devegowda D, Sigal R (2016). A microscopic characterization of wettability in shale kerogen with varying maturity levels. J Nat Gas Sci Eng, 33: 1078–1086

Hu Y N, Devegowda D, Striolo A, Van Phan A T, Ho T A, Civan F (2015). Microscopic dynamics of water and hydrocarbon in shale-kerogen pores of potentially mixed wettability. SPE J, 20(1): 112–124

Jia C Z, Zheng M, Zhang Y F (2012). Unconventional hydrocarbon resources in China and the prospect of exploration and development. Pet Explor Dev, 39(2): 139–146

Jiang S, Tang X L, Cai D S, Xue G, He Z L, Long S X, Peng Y M, Gao B, Xu Z Y, Dahdah N (2017). Comparison of marine, transitional, and lacustrine shales: a case study from the Sichuan Basin in China. J Petrol Sci Eng, 150: 334–347

Korb J P, Nicot B, Louis-Joseph A, Bubici S, Ferrante G (2014). Dynamics and wettability of oil and water in oil shales. J Phys Chem C, 118(40): 23212–23218

Lahn L, Bertier P, Seemann T, Stanjek H (2020). Distribution of sorbed water in the pore network of mudstones assessed from physisorption measurements. Microporous Mesoporous Mater, 295: 109902

Li J, Li X F, Wang X Z, Li Y Y, Wu K L, Shi J T, Yang L, Feng D, Zhang T, Yu P L (2016). Water distribution characteristic and effect on methane adsorption capacity in shale clay. Int J Coal Geol, 159: 135–154

Li J, Li X F, Wu K L, Feng D, Zhang T, Zhang Y F (2017). Thickness and stability of water film confined inside nanoslits and nanocapillaries of shale and clay. Int J Coal Geol, 179: 253–268

Li J, Tang S H, Zhang S H, Li L, Wei J G, Xi Z D, Sun K (2018). Characterization of unconventional reservoirs and continuous accumulations of natural gas in the Carboniferous-Permian strata, mid-eastern Qinshui Basin, China. J Nat Gas Sci Eng, 49: 298–316

Liang J T, Huang W H, Wang H L, Blum M J, Chen J, Wei X L, Yang G Q (2020). Organic geochemical and petrophysical characteristics of transitional coal-measure shale gas reservoirs and their relationships with sedimentary environments: a case study from the Carboniferous-Permian Qinshui Basin, China. J Petrol Sci Eng, 184: 106510

Liang Q S, Zhang X, Tian J C, Sun X, Chang H L (2018). Geological and geochemical characteristics of marine-continental transitional shale from the Lower Permian Taiyuan Formation, Taikang Uplift, southern North China Basin. Mar Pet Geol, 98: 229–242

Liu H L, Wang H Y (2013). Ultra-low water saturation characteristics and the identification of over-pressured play fairways of marine shales in south China. Nat Gas Ind, 33(7): 140–144 (in Chinese)

Liu J C, Monson P A (2005). Does water condense in carbon pores? Langmuir, 21(22): 10219–10225

Liu M (2016). Upper Paleozoic shale gas reservoiring features and resource potential assessment in Qinshui Basin. Coal Geol China, 28(12): 25–33 (in Chinese)

Löhr S C, Baruch E T, Hall P A, Kennedy M J (2015). Is organic pore development in gas shales influenced by the primary porosity and structure of thermally immature organic matter? Org Geochem, 87: 119–132

Mahadevan J, Sharma M, Yortsos Y C (2007). Water removal from porous media by gas injection: experiments and simulation. Transp Porous Media, 66(3): 287–309

McCutcheon A L, Barton W A (1999). Contribution of mineral matter to water associated with bituminous coals. Energy Fuels, 13(1): 160–165

Men X Y, Wang L X, Wang Y, Lou Y, Guo W (2021). Strategic pattern of China's oil and gas exploration and development in the new era and prospects for 2035. China Petroleum Exploration, 26(3): 1–8 (in Chinese)

Merkel A, Fink R, Littke R (2015). The role of pre-adsorbed water on methane sorption capacity of Bossier and Haynesville shales. Int J Coal Geol, 147–148: 1–8

Miller M, Shanley K (2010). Petrophysics in tight gas reservoirs — key challenges still remain. The Leading Edge (Special Section): Tight gas sands, 1464–1469

Newsham K E, Rushing J A, Lasswell P M (2003). Use of vapor desorption data to characterize high vapillary pressures in a basin-centered gas accumulation with ultra-low water saturations. In: SPE Annual Technical Conference and Exhibition, October 2003, Denver, Colorado

Odusina E, Sondergeld D C, Rai D C (2011). An NMR study on shale wettability. In: Canadian Unconventional Resources Conference, November 2011, Calgary, Alberta, Canada

Passey Q R, Bohacs K M, Esch W L, Klimentidis R, Sinha S (2010). From oil-prone source rock to gas-producing shale reservoir - geologic and petrophysical characterization of unconventional shale-gas reservoirs. In: SPE International Oil and Gas Conference and Exhibition in China, June 2010, Beijing, China

Qin Y, Liang J S, Shen J, Liu Y H, Wang C W (2014). Gas logging shows and gas reservoir types in tight sandstones and shales from Southern Qinshui Basin. J China Coal Soci, 39(8): 1559–1565 (in Chinese)

Ren Z L, Xiao H, Liu L, Zhang S, Qin Y, Wei C T (2005). The evidence of fission-track data for the study of tectonic thermal history in Qinshui Basin. Chin Sci Bull, 50(S1): 104–110

Ross D J K, Bustin R M (2009). The importance of shale composition and pore structure upon gas storage potential of shale gas reservoirs. Mar Pet Geol, 26(6): 916–927

Seemann T, Bertier P, Krooss B M, Stanjek H (2017). Water vapour sorption on mudrocks. Spec Publ Geol Soc Lond, 454(1): 201–233

Sondergeld C H, Newsham K E, Comisky J T, Rice M C, Rai C S (2010). Petrophysical considerations in evaluating and producing shale gas resources. In: SPE Unconventional Gas Conference, February 23–25, Pittsburgh, Pennsylvania, USA

Song Y, Ma X Z, Liu S B, Jiang L, Hong F, Qin Y (2019). Gas accumulation conditions and key exploration and development technologies in Qinshui coalbed methane field. Acta Petrol Sin, 40(5): 621–634 (in Chinese)

Striolo A, Naicker P K, Chialvo A A, Cummings P T, Gubbins K E (2005). Simulated water adsorption isotherms in hydrophilic and

hydrophobic plunger nanopores. Adsorption, 11(S1): 397–401

Su X B, Lin X Y, Zhao M J, Song Y, Liu S B (2005). The Upper Paleozoic coalbed methane system in the Qinshui Basin, China. AAPG Bull, 89(1): 81–100

Sun J, Xiao X M, Wei Q, Cheng P, Tian H (2020b). Occurrence of irreducible water and its influences on gas-bearing property of gas shales from shallow Longmaxi Formation in the Xishui Area, Guizhou, southern China. Front Earth Sci, 9: 22966463

Sun J, Xiao X M, Wei Q, Cheng P, Tian H, Wu Y W (2020a). Gas in place and its controlling factors of the shallow Longmaxi shale in the Xishui area, Guizhou, China. J Nat Gas Sci Eng, 77: 103272

Thommes M, Kaneko K, Neimark A V, Olivier J P, Rodriguez-Reinoso F, Rouquerol J, Sing K S W (2015). Physisorption of gases, with special reference to the evaluation of surface area and pore size distribution (IUPAC Technical Report). Pure Appl Chem, 87(9–10): 1051–1069

Tian H, Pan L, Zhang T W, Xiao X M, Meng Z P, Huang B J (2015). Pore characterization of organic-rich Lower Cambrian shales in Qiannan Depression of Guizhou Province, southwestern China. Mar Pet Geol, 62: 28–43

Wardlaw N C, McKellar M (1998). Wettability and connate water saturation in hydrocarbon reservoirs with bitumen deposits. J Nat Gas Sci Eng, 20: 141–146

Wei Z H, Wei X F (2014). Comparison of gas-bearing property between different pore types of shales: a case from the Upper Ordovician Wufeng and Longmaxi formations in the Jiaoshiba area, Sichuan, China. Nat Gas Ind, 34(6): 37–41 (in Chinese)

Wen H, Chen M, Jin Y, Zhang Y Y, Ge W F, Du J L, Zeng C (2015). Water activity characteristics of deep brittle shale from southwest China. Appl Clay Sci, 108: 165–172

Wu K, Chen Z, Li J, Li X, Xu J, Dong X (2017). Wettability effect on nanoconfined water flow. Proc Natl Acad Sci USA, 114(13): 3358–3363

Wu P, Aguilera R (2012). Investigation of gas shales at nanoscale using Scan Electron Microscopy, Transmission Electron Microscopy and Atomic Force Microscopy, and up-scaling to a petrophysical model for water saturation evaluation in shales. In: SPE Annual Technical Conference and Exhibition, October 8–10, San Antonio, Texas, USA

Yang C, Zhang J C, Tang X, Ding J H, Zhao Q R, Dang W, Chen H Y, Su Y, Li B W, Lu D F (2017). Comparative study on micro-pore structure of marine, terrestrial, and transitional shales in key areas, China. Int J Coal Geol, 171: 76–92

Yang R, Jia A Q, He S, Hu Q H, Dong T, Hou Y G, Yan J P (2020). Water adsorption characteristics of organic-rich Wufeng and Longmaxi Shales, Sichuan Basin (China). J Petrol Sci Eng, 193: 107387

Zhang J C, Jiang S L, Tang X, Zhang P X, Tang Y, Jin T Y (2009). Accumulation types and resources characteristics of shale gas in China. Nat Gas Ind, 29: 109–114 (in Chinese)

Zhang J, Chenevert M E, Al-Bazali T, Sharma M M (2004). A new gravimetric-swelling test for evaluating water and ion uptake in shales. In: SPE Annual Technical Conference and Exhibition, 26–29 September, Houston, Texas, USA

Zhang M, Fu X H, Zhang Q H, Cheng W P (2019a). Research on the organic geochemical and mineral composition properties and its influence on pore structure of coal-measure shales in Yushe-Wuxiang Block, south central Qinshui Basin, China. J Petrol Sci Eng, 173: 1065–1079

Zhang Q, Xiong X L, Pang Z L, Liu R H, Liang F, Liang P P, Guo W, Zhang J C (2019b). Composition effects on pore structure of transitional shale: a case study of the upper Carboniferous Taiyuan Formation in the eastern uplift of the Liaohe Depression, China. Mar Pet Geol, 110: 638–649

Zolfaghari A, Dehghanpour H, Holyk J (2017). Water sorption behaviour of gas shales: I. role of clays. Int J Coal Geol, 179: 130–138

Zou C N, Dong D Z, Wang Y M, Li X J, Huang J L, Wang S F, Guan Q Z, Zhang C C, Wang H Y, Liu H L, Bai W H, Liang F, Lin W, Zhao Q, Liu D X, Yang Z, Liang P P, Sun S S, Qiu Z (2016). Shale gas in China: characteristics, challenges and prospects (II). Pet Explor Dev, 43(2): 182–196

Zou C N, Pan S Q, Jing Z H, Gao J L, Yang Z, Wu S T, Zhao Q (2020a). Shale oil and gas revolution and its impact. Acta Petrol Sin, 41(1): 1–11 (in Chinese)

Zou J, Rezaee R, Yuan Y J, Liu K Q, Xie Q, You L J (2020b). Distribution of adsorbed water in shale: an experimental study on isolated kerogen and bulk shale samples. J Petrol Sci Eng, 187: 106858